

1 **Technical Note: Nighttime OH and HO₂ chemical equilibria in the mesosphere – lower**
2 **thermosphere**

3 Mikhail Yu. Kulikov^{1,2}, Mikhail V. Belikovich^{1,2}, Aleksey G. Chubarov^{1,2}, Svetlana O. Dementyeva¹, and
4 Alexander M. Feigin^{1,2}

5 ¹A. V. Gaponov-Grekhov Institute of Applied Physics of the Russian Academy of Sciences, 46 Ulyanov
6 Str., 603950 Nizhny Novgorod, Russia

7 ²Lobachevsky State University of Nizhny Novgorod, 23 Gagarin Avenue, Nizhny Novgorod, Russia,
8 603022

9 Correspondence to: Mikhail Yu. Kulikov (mikhail_kulikov@mail.ru)

10
11 **Abstract.** At the altitudes of the mesosphere – lower thermosphere OH and HO₂ play a significant
12 role in many physicochemical processes. Thus, monitoring their spatiotemporal evolution together with
13 other chemically active trace gases is one of the most important problems for this atmosphere region, in
14 which direct measurements are difficult. The paper studies the nighttime OH and HO₂ chemical equilibria
15 using the 3D chemical transport modeling within the general approach, which includes the identification
16 of the main sources and sinks in the equilibrium space-time areas and derivation of analytical criteria for
17 equilibrium validity. The presented analysis shows, that there are extended areas, where nighttime HO₂
18 and OH are close to their local equilibrium concentrations, determined mainly by the reaction between
19 HO_x – O_x components among themselves and with H₂O₂, N, NO, NO₂ and CO. In the upper mesosphere –
20 lower thermosphere the equilibrium expressions can be shortened, so that they include the HO_x – O_x
21 chemistry only. These expressions describe the HO₂ and OH equilibria from the top down to some
22 boundaries, the altitude positions of which vary in the interval between 72-73 and 85 km and depend
23 essentially on season and latitude. The developed analytical criteria almost everywhere reproduce well the
24 main features of these boundaries. Due to weak sensitivity to uncertainties of reaction rates and other
25 parameters, the criteria can be considered a robust instrument for HO₂ and OH equilibrium validation.
26 The obtained results allow us to extend previously proposed methods for the retrieval of poorly measured
27 components from measurement data and to develop new approaches.

29 **1 Introduction**

30 Monitoring the spatiotemporal evolution of chemically active trace gases is one of the most
31 important problems in atmospheric research. Despite the increase of the experimental data volume
32 nowadays, primarily due to the development in remote sensing methods, many important trace gases
33 continue to be unavailable for direct and regular measurements. A well-known way to increase the
34 information content of experimental campaigns is to use the available experimental data in conjunction
35 with a certain chemical or physicochemical model to derive unmeasured characteristics indirectly. Within
36 the framework of this approach, the model acts as *a priori* relationship between directly measured and
37 retrieved characteristics. The simplest model, that makes it possible to implement this approach, is based
38 on the condition of local (in both time and space) photochemical/chemical balance (local equilibrium)
39 between sources and sinks of the so-called “fast” components: trace gases with short lifetimes relatively,
40 in particular, to the characteristic transport times. Mathematically this condition does not mean that the
41 fast variables are at equilibrium, but when it is fulfilled, the corresponding concentrations are close to
42 their instantaneous equilibrium values. At the same time due to the strong dissipation in most cases
43 (except the special cases where the ensemble of fast components includes the slow family of these
44 components), there is no need to follow the law of matter conservation. It is possible to disregard
45 insignificant sinks and sources, including those caused by transport, in the corresponding balance
46 equations without the loss of accuracy. The resulting algebraic equations are the simplest *a priori* local
47 relations between measurable and retrieved trace gases. These relationships can be used to derive
48 information about hard-to-measure atmospheric species, determine key atmospheric characteristics (for
49 example, temperature (Marchand et al., 2007)), validate the data quality of simultaneous measurements of
50 several atmospheric components (Kulikov et al., 2018a), estimate reaction rate constants (Stedman et al.,
51 1975; Avallone and Toohey, 2001), evaluate sources/sinks (Cantrell et al., 2003), etc.

52 For several decades the photochemical/chemical equilibrium approximation has been used to solve
53 many atmospheric tasks. It is applied (see, e.g., the short review in Kulikov et al. (2018a) and references
54 therein) in investigations of the surface layer and free troposphere chemistry in different regions (over
55 megapolises, in rural areas, in the mountains, over the seas), in stratospheric chemistry studies, including
56 derivation of critical parameters in the ozone destruction catalytic cycles, and in studies of the HO_x – O_x
57 chemistry and airglows (O(¹S) green-line, O₂ A-band, OH Meinel band emissions) at the heights of the
58 mesosphere – lower thermosphere. In the latter case the distributions of unmeasured characteristics are
59 determined from the data of daytime and nighttime rocket and satellite measurements (e.g., Evans and
60 Llewellyn, 1973; Good, 1976; Pendleton et al., 1983; McDade et al., 1985; McDade and Llewellyn, 1988;
61 Evans et al., 1988; Thomas, 1990; Llewellyn et al., 1993; Llewellyn and McDade, 1996; Russell and
62 Lowe, 2003; Russell et al., 2005; Kulikov et al., 2006, 2009, 2017, 2022a, 2022b; Mlynczak et al., 2007,

63 2013a, 2013b, 2014, 2018; Smith et al., 2010; Xu et al., 2012; Siskind et al., 2008, 2015; Fytterer et al.,
64 2019) with the use of equilibrium assumptions for ozone and excited states of OH, O, and O₂. For
65 example, such an approach is applied to the data of the SABER (Sounding of the Atmosphere using
66 Broadband Emission Radiometry) instrument onboard the TIMED (Thermosphere Ionosphere
67 Mesosphere Energetics and Dynamics) satellite, which since 2002 continues to measure simultaneous
68 profiles of temperature, ozone and volume emission rates of OH* transitions in wide ranges of altitude,
69 local time and latitude with a rather high space-time resolution.

70 Note a number of general aspects of the application of equilibrium conditions in the above
71 examples. First of all, there are no clear criteria, indicating the conditions under which the use of
72 equilibrium approximation is justified. Usually a certain component is taken to be a fast variable, if its
73 lifetime is much shorter, than the lifetimes of other components of studied photochemical/chemical
74 system or the duration of a day, daytime, nighttime, etc. For example, in the papers on SABER data
75 processing (Mlynczak et al., 2013a, 2013b, 2014, 2018) it is assumed, that the nighttime ozone chemical
76 equilibrium in the mesopause is well fulfilled at altitudes of 80–100 km, since the nighttime ozone
77 lifetime at these altitudes varies in the range from several minutes to several tens of minutes. Note, that
78 this assumption is quite popular and used in different tasks (e.g., Swenson and Gardner, 1998; Marsh et
79 al., 2006; Smith et al., 2009; Nikoukar et al., 2007; Xu et al., 2010, 2012; Kowalewski et al., 2014;
80 Grygalashvyly et al., 2014; Grygalashvyly, 2015; Sonnemann et al., 2015; Kulikov et al., 2021).
81 Belikovich et al. (2018) and Kulikov et al. (2018b, 2019, 2023a) analyzed the nighttime ozone chemical
82 equilibrium numerically, analytically, and with the use of SABER/TIMED data. It was revealed, that the
83 short lifetime is not a sufficient condition, so, this equilibrium may be significantly disturbed above 80
84 km. The local ratio between true and equilibrium concentrations may vary widely and reach up to several
85 orders of magnitude (e.g., Figure 5 in Kulikov et al. (2018b)). Thus, without special restrictions the error
86 in retrieved characteristics due to the use of equilibrium approximation is uncontrollable and may
87 significantly exceed all other errors in the retrieval procedure due to, for example, uncertainties in the
88 measurement data and rate constants.

89 Since the papers of Belikovich et al. (2018) and Kulikov et al. (2018b, 2019, 2023a), we developed
90 the general approach to correctly identify fast components, employing the data from a global 3D chemical
91 transport model. It includes:

- 92 1. Plotting of the equilibrium space-time maps of the components of interest.
- 93 2. Identification of the main sources and sinks in the found equilibrium areas.
- 94 3. Derivation and subsequent use of analytical criteria that make it possible to determine the fulfillment of
95 the equilibrium condition locally (in time and space) with the use of the measurement data only.

96 The latter point is based on the theory of chemical equilibrium of a certain trace gas, acquired from
97 estimations of its lifetime and equilibrium concentration, and time dependences of these characteristics
98 (Kulikov et al., 2023a). Note, that when equilibrium condition is applied to measurement data in the
99 retrieval of unmeasured characteristics, the criterion allows controlling and limiting the possible error
100 caused by the equilibrium approximation.

101 The main goal of the paper is to apply this approach to the analysis of nighttime OH and HO₂
102 chemical equilibria in the mesosphere – lower thermosphere. Along with O and H, OH and HO₂ are
103 important components of HO_x – O_x chemistry, participating (a) in chemical heating through, in particular,
104 O+OH → O₂+H and O+HO₂ → O₂+OH exothermic reactions, (b) in formation of airglows, (c) in
105 catalytic cycles of the ozone destruction. Moreover, the equilibrium conditions of OH and HO₂ are
106 additional *a priori* relationships, that can be used to retrieve these components or other characteristics
107 from measured data. In particular, Panka et al. (2021) proposed the method for nighttime total OH
108 retrieval from SABER/TIMED data at 80-100 km, which does not use the ozone chemical equilibrium.
109 However, the method applies the equilibrium between sources and sinks not only to excited states of OH
110 with ultrashort lifetimes, but also to the ground state. Therefore, this point is verified in our paper.

111 In the next section we present the used model and methods. In Section 3 the model data are used to
112 plot HO₂ and OH equilibrium maps. In Sections 4-5 we identify the main reactions, determining
113 equilibria of these gases, and present their shortened equilibria conditions at the upper mesosphere and
114 lower thermosphere altitudes. In Section 6 the criteria for HO₂ and OH equilibria validity are developed.
115 In Section 7 we discuss the obtained results and their possible applications.

116

117 **2 Used 3D model and Approaches**

118 The analysis of OH and HO₂ nighttime chemical equilibria was carried out, using the data, obtained
119 with calculation of 3D chemical transport model of the middle atmosphere, developed at the Leibniz
120 Institute of Atmospheric Physics (e.g., Sonnemann et al., 1998; Körner & Sonnemann, 2001;
121 Grygalashvyly et al., 2009; Hartogh et al., 2004, 2011) to investigate the mesosphere – lower
122 thermosphere chemistry, in particular, in the extended mesopause region. A number of papers (e.g.,
123 Hartogh et al., 2004, 2011; Sonnemann, et al., 2006, 2008) validated the model with measurements, in
124 particular, for ozone and water vapor.

125 The space-time distribution of temperature and winds were taken from the model of the dynamics
126 of the middle atmosphere COMMA-IAP (e.g., Kremp et al., 1999; Berger and von Zahn, 1999) with an
127 updated frequency of 1 day and linear smoothing between subsequent updates to avoid unrealistic jumps

128 in the calculated concentrations of trace gases. 3D advective transport is taken into account with the use
 129 of the Walcek-scheme (Walcek, 2000). The vertical diffusive transport (turbulent and molecular) is
 130 calculated with the use of the implicit Thomas algorithm (Morton and Mayers, 1994). The model grid has
 131 118 pressure-height levels (0–135 km), 16 latitudinal and 32 longitudinal levels. The chemical module
 132 (see Table 1) comprises 25 constituents (O, O(¹D), O₃, H, OH, HO₂, H₂O₂, H₂O, H₂, N, NO, NO₂, NO₃,
 133 N₂O, CH₄, CH₂, CH₃, CH₃O₂, CH₃O, CH₂O, CHO, CO, CO₂, O₂, N₂), 54 chemical reactions between
 134 them and 15 photo-dissociation reactions. The model utilizes the pre-calculated dissociation rates (Kremp
 135 et al., 1999) and their dependence on the altitude and solar zenith angle.

136 The model was used to calculate a one-year global evolution of the above mentioned trace gases. To
 137 remove the transition regions corresponding to sunset and sunrise, we use only local times when the solar
 138 zenith angle $\chi > 105^\circ$. As a result, we find the spatiotemporal series of the OH/OH^{eq} and HO_2/HO_2^{eq}
 139 ratios. Here OH and HO_2 are the local nighttime values of hydroxyl and hydroperoxyl radicals, calculated
 140 by the model, OH^{eq} and HO_2^{eq} are their local equilibrium values, corresponding to the instantaneous
 141 balance between production and loss terms respectively. To determine each local value of OH^{eq} and
 142 HO_2^{eq} we used the local values of the parameters (temperature, O₂, and N₂) and the concentrations of
 143 other trace gases, determining local chemical sources and sinks of OH and HO_2 . Then the OH/OH^{eq} and
 144 HO_2/HO_2^{eq} series were averaged over the zonal coordinate and time during each month and were
 145 presented as height-latitude maps, depending on the month. Each map contains lines, marking the
 146 boundaries of the equilibrium areas, where the following conditions are satisfied:

$$147 \left\{ \begin{array}{l} |\langle OH/OH^{eq} \rangle - 1| \leq 0.1 \\ \sigma_{OH/OH^{eq}} \leq 0.1 \end{array} \right\}, \left\{ \begin{array}{l} |\langle HO_2/HO_2^{eq} \rangle - 1| \leq 0.1 \\ \sigma_{HO_2/HO_2^{eq}} \leq 0.1 \end{array} \right\}, \quad (1)$$

148 where the angle brackets are used to denote the values averaged in time and space, $\sigma_{OH/OH^{eq}}$ and
 149 $\sigma_{HO_2/HO_2^{eq}}$ are standard deviations of the OH/OH^{eq} and HO_2/HO_2^{eq} ratios from 1 respectively.

150 Then we plotted spatiotemporal maps, showing the relative contribution of each reaction to a
 151 summarized source or sink at all altitudes and latitudes. These maps helped us to identify the main
 152 sources and sinks, describing the chemical equilibrium of nighttime OH and HO₂ in the equilibrium areas
 153 to an accuracy of better than a few percent.

154 Finally, we obtained and verified the analytical criteria of OH and HO₂ nighttime chemical
 155 equilibria according to Kulikov et al. (2023a). The paper considered the pure chemical evolution of a
 156 certain trace gas n :

$$157 \frac{dn}{dt} = I_n - S_n = -\frac{1}{\tau_n}(n - n^{eq}),$$

158
$$\tau_n = \frac{n}{S_n}, \quad n^{eq} = \frac{n \cdot I_n}{S_n}, \quad (2)$$

159 where t is time, I_n and S_n are total photochemical/chemical sources and sinks of n respectively, τ_n is the
 160 n lifetime and n^{eq} is its equilibrium concentration, corresponding to the condition $I_n = S_n$. The lifetime
 161 determines the characteristic time scale, for which n approaches n^{eq} , when $n^{eq} = const$. In general case
 162 τ_n and n^{eq} are functions of time. Kulikov et al. (2023a) showed strictly mathematically, that the local
 163 values of n and n^{eq} are close to each other ($n(t) \approx n^{eq}(t)$), when $\tau_n \ll \tau_{n^{eq}}$, where $\tau_{n^{eq}}$ is the local time
 164 scale of n^{eq} :

165
$$\tau_{n^{eq}} \equiv \frac{n^{eq}}{|dn^{eq}/dt|}. \quad (3)$$

166 The expression for τ_n is found from the total sink of n . The expression for $\tau_{n^{eq}}$ is derived from Eq. (3)
 167 with the use of differential equations, describing chemical evolution of other reacting components, which
 168 determine the expression for n^{eq} . Kulikov et al. (2023a) also showed, when $\tau_n \ll \tau_{n^{eq}}$, $n \cong n^{eq} (1 -$
 169 $sign(\frac{dn^{eq}}{dt}) \cdot \frac{\tau_n}{\tau_{n^{eq}}})$ in the first order approximation. Thus, the criterion

170
$$\tau_n / \tau_{n^{eq}} \leq 0.1 \quad (4)$$

171 is sufficient, in order to the possible relative difference between n and n^{eq} to be no more than 0.1.

172

173 **3 Nighttime HO₂ and OH chemical equilibria**

174 According to the Table 1 HO₂ chemical sources in nighttime are determined by the following
 175 reactions:

176 $H+O_2+M \rightarrow HO_2+M$ (R20), $OH+O_3 \rightarrow O_2+HO_2$ (R22), $H_2O_2+OH \rightarrow H_2O+HO_2$ (R29), $H_2O_2+O \rightarrow$
 177 $OH+HO_2$ (R19), $CHO+O_2 \rightarrow HO_2+CO$ (R40), $CH_3O+O_2 \rightarrow CH_2O+HO_2$ (R37),

178 whereas chemical sinks of this component are as follows:

179 $HO_2+O \rightarrow OH+O_2$ (R18), $HO_2+O_3 \rightarrow OH+2O_2$ (R23), $OH+HO_2 \rightarrow H_2O+O_2$ (R28), $H+HO_2 \rightarrow 2OH$
 180 (R14), $H+HO_2 \rightarrow H_2O+O$ (R15), $H+HO_2 \rightarrow H_2+O_2$ (R16), $NO+HO_2 \rightarrow NO_2+OH$ (R50), $HO_2+HO_2 \rightarrow$
 181 $H_2O_2+O_2$ (R30), $HO_2+HO_2+M \rightarrow H_2O_2+O_2+M$ (R31).

182 Thus, HO₂ local equilibrium concentration is described by the following equation:

183
$$HO_2^{eq} = \frac{k_{20} \cdot H \cdot M \cdot O_2 + k_{22} \cdot OH \cdot O_3 + k_{29} \cdot H_2O_2 \cdot OH + k_{19} \cdot H_2O_2 \cdot O + k_{40} \cdot CHO \cdot O_2 + k_{37} \cdot CH_3O \cdot O_2}{k_{18} \cdot O + k_{23} \cdot O_3 + k_{28} \cdot OH + (k_{14} + k_{15} + k_{16}) \cdot H + k_{50} \cdot NO + 2 \cdot (k_{30} + k_{31} \cdot M) \cdot HO_2} \quad (5)$$

184 Figure 1 plots height-latitude cross sections for the $\langle HO_2/HO_2^{eq} \rangle$ ratio for each month. The
 185 black solid lines mark the boundaries of equilibrium areas, where according to condition (1) local values
 186 of HO_2 are close to their equilibrium values with a possible bias of less than 10%. At low and middle
 187 latitudes one can see the presence of the main equilibrium area, which extends from the top of the
 188 analyzed altitude range to the lower boundary. The height of this equilibrium boundary, $z_{HO_2^{eq}}$, depends
 189 on the season and latitude and varies in the interval between 73 and 85 km. It is the highest and the lowest
 190 during the summer and winter respectively at the middle latitudes. Near the equator $z_{HO_2^{eq}}$ demonstrates
 191 the weakest annual variations and varies in the 81-83 km range. There are local areas below the upper
 192 longest black line, but they are small and irregular and can be omitted from our consideration. Note that
 193 the maps show the existence of equilibrium near 50 km, which can be assumed to be the beginning of the
 194 main equilibrium area in the stratosphere. At high latitudes there is the main equilibrium area as at low
 195 and middle latitudes, but this area above 70-75° of latitude can extend down to 50 km.

196 In accordance to the Table 1 OH chemical sources are determined by the following reactions:

197 $H+O_3 \rightarrow OH+O_2$ (R21), $HO_2+O \rightarrow OH+O_2$ (R18), $HO_2+O_3 \rightarrow OH+2O_2$ (R23), $H+HO_2 \rightarrow 2OH$ (R14),
 198 $NO+HO_2 \rightarrow NO_2+OH$ (R50), $H_2O_2+O \rightarrow OH+HO_2$ (R19), $H+NO_2 \rightarrow OH+NO$ (R51), $O(^1D)+H_2O \rightarrow$
 199 $2OH$ (R7), $O(^1D)+H_2 \rightarrow H+OH$ (R8), $CH_4+O(^1D) \rightarrow CH_3+OH$ (R9),

200 whereas chemical sinks of this component are as follows:

201 $OH+O \rightarrow H+O_2$ (R17), $OH+O_3 \rightarrow O_2+HO_2$ (R22), $OH+HO_2 \rightarrow H_2O+O_2$ (R28), $OH+OH \rightarrow H_2O+O$
 202 (R26), $OH+OH+M \rightarrow H_2O_2+M$ (R27), $H+OH+N_2 \rightarrow H_2O+N_2$ (R24), $H_2O_2+OH \rightarrow H_2O+HO_2$ (R29),
 203 $OH+CO \rightarrow H+CO_2$ (R32), $CH_4+OH \rightarrow CH_3+H_2O$ (R33), $OH+H_2 \rightarrow H_2O+H$ (R25), $N+OH \rightarrow NO+H$
 204 (R49).

205 Thus, OH local equilibrium concentration is described by the following equation:

$$\begin{aligned}
 206 \quad OH^{eq} = & (k_{21} \cdot H \cdot O_3 + k_{18} \cdot O \cdot HO_2 + k_{23} \cdot HO_2 \cdot O_3 + 2 \cdot k_{14} \cdot H \cdot HO_2 + k_{50} \cdot HO_2 \cdot NO + k_{19} \cdot \\
 207 \quad & H_2O_2 \cdot O + k_{24} \cdot H \cdot N_2 + k_{51} \cdot NO_2 \cdot H + 2 \cdot k_7 \cdot O(^1D) \cdot H_2O + k_8 \cdot O(^1D) \cdot H_2 + k_9 \cdot O(^1D) \cdot \\
 208 \quad & CH_4) / (k_{17} \cdot O + k_{22} \cdot O_3 + k_{28} \cdot HO_2 + 2 \cdot (k_{26} + k_{27} \cdot M) \cdot OH + k_{29} \cdot H_2O_2 + k_{32} \cdot CO + k_{33} \cdot CH_4 + \\
 209 \quad & k_{25} \cdot H_2 + k_{25} \cdot N) \quad (6)
 \end{aligned}$$

210 Figure 2 shows height-latitude cross sections for the $\langle OH/OH^{eq} \rangle$ ratio for each month. In this
 211 case the equilibrium covers up to 70-80% of the presented ranges of heights and latitudes, so that the
 212 black solid lines mark the external boundaries of non-equilibrium areas. In March and September this
 213 area is almost symmetrical to the equator. In April-August it is shifted towards the northern hemisphere.
 214 In October-February this area is higher in the southern hemisphere. In all months it is below 85-86 km. In

215 the polar regions there are latitudinal ranges, where OH is close to equilibrium throughout the entire range
 216 of heights.

217

218 **4 The main reactions, determining HO₂ and OH equilibria**

219 Figure 3 presents height-latitude contour maps, showing the relative contribution of a certain
 220 reaction to the total source and sink of HO₂ in January, taken as an example. To increase the information
 221 content of the panels, the altitude range is cut off everywhere to 10⁻³ hPa, since there are no significant
 222 changes above. Note firstly, that reaction H+O₂+M → HO₂+M determines a major (up to 95% and more)
 223 contribution in the main equilibrium area almost everywhere, except for the polar regions above 70-75° of
 224 latitude and below 75-80 km, where the reactions OH+O₃ → O₂+HO₂ and H₂O₂+OH → H₂O+HO₂
 225 become important and should be taken into account. Other reactions (H₂O₂+O → OH+HO₂, CHO+O₂ →
 226 HO₂+CO, CH₃O+O₂ → CH₂O+HO₂) together contribute less than 2-3% to the total source of HO₂ in the
 227 main equilibrium area and may be omitted. Secondly, the reaction HO₂+O → OH+O₂ determines a major
 228 (up to 95% and more) contribution to the total sink in the main equilibrium area almost everywhere,
 229 except for the same small polar areas, as in the considered case with the sources, where the reactions
 230 HO₂+O₃ → OH+2O₂ and NO+HO₂ → NO₂+OH are important and should be taken into account. The
 231 reactions OH+HO₂ → H₂O+O₂, H+HO₂ → 2OH, H+HO₂ → H₂O+O, and H+HO₂ → H₂+O₂ contribute
 232 cumulatively up to 10-15% of the total sink near the boundary of the main equilibrium area. The
 233 remaining reactions (HO₂+HO₂ → H₂O₂+O₂, HO₂+HO₂+M → H₂O₂+O₂+M) are not important in the
 234 main equilibrium area and can be omitted. The complete figures for HO₂ sources and sinks for every
 235 month (all 12 panels) are given in Supplement (Figs. S3-S11).

236 Therefore, the expression for HO₂ local equilibrium concentration can be simplified as follows:

$$237 \quad HO_2^{eq} = \frac{k_{20} \cdot H \cdot M \cdot O_2 + k_{22} \cdot OH \cdot O_3 + k_{29} \cdot H_2O_2 \cdot OH}{k_{18} \cdot O + k_{23} \cdot O_3 + k_{28} \cdot OH + (k_{14} + k_{15} + k_{16}) \cdot H + k_{50} \cdot NO} \quad (7)$$

238 Figure 4 presents height-latitude contour maps, showing the relative contribution of a certain
 239 reaction to the total source and sink of OH in January, taken as an example in Figure 3. As in the previous
 240 case, the altitude range is cut off at 10⁻³ hPa, because only the panels for the reactions H+O₃ → OH+O₂
 241 and HO₂+O → OH+O₂ consist of interesting variations above. Note, that firstly these reactions are the
 242 main OH sources in the upper part of the presented distributions down to 70-75 km, where they jointly
 243 provide up to a 95% contribution to the equilibrium concentration. Also the reaction HO₂+O₃ → OH+2O₂
 244 is major source in the lower part of the presented distribution from 50 to 60-70 km. The reaction
 245 NO+HO₂ → NO₂+OH is important around non-equilibrium areas of OH and should be taken into
 246 account, whereas the reaction H +NO₂ → OH+NO is important in compact altitude-latitude areas near the

247 poles, the reaction $H+HO_2 \rightarrow 2OH$ gives up to 10-15% contribution in small areas near the equilibrium
 248 boundary. Other reactions ($O(^1D)+H_2O \rightarrow 2OH$, $O(^1D)+H_2 \rightarrow H+OH$, $CH_4+O(^1D) \rightarrow CH_3+OH$, H_2O_2+O
 249 $\rightarrow OH+HO_2$) together contribute less than 2-3% of the total source of OH in the main equilibrium area
 250 and can be omitted. Secondly, the reaction $OH+O \rightarrow H+O_2$ is the main OH sink in the upper part of the
 251 presented distributions down to 70-80 km, where it provides up to 95% of the equilibrium concentration.
 252 The reactions $OH+CO \rightarrow H+CO_2$ and $OH+O_3 \rightarrow O_2+HO_2$ are major in the lower part of the presented
 253 distributions from 50 to 70-80 km. The reaction $OH+HO_2 \rightarrow H_2O+O_2$ is significant enough around non-
 254 equilibrium areas of OH, whereas the reaction $H_2O_2+OH \rightarrow H_2O+HO_2$ is important in the compact
 255 altitude-latitude area near the poles. Other reactions ($OH+OH \rightarrow H_2O+O$, $OH+H_2 \rightarrow H_2O+H$, $N+OH \rightarrow$
 256 $NO+H$, $CH_4+OH \rightarrow CH_3+H_2O$, $H+OH+N_2 \rightarrow H_2O+N_2$, $OH+OH+M \rightarrow H_2O_2+M$) together contribute
 257 less than 2-3% to the total sink of OH in the main equilibrium area and can be omitted. The complete
 258 figures for OH sources and sinks for every month (all 12 panels) are given in Supplement (Figs. S12-
 259 S24).

260 Therefore, the expression for OH local equilibrium concentration can be simplified as follows:

$$261 \quad OH^{eq} = \frac{k_{21} \cdot H \cdot O_3 + k_{18} \cdot O \cdot HO_2 + k_{23} \cdot HO_2 \cdot O_3 + 2 \cdot k_{14} \cdot H \cdot HO_2 + k_{24} \cdot H \cdot N_2 + k_{50} \cdot HO_2 \cdot NO + k_{51} \cdot NO_2 \cdot H}{k_{17} \cdot O + k_{22} \cdot O_3 + k_{28} \cdot HO_2 + k_{29} \cdot H_2O_2 + k_{32} \cdot CO} \quad (8)$$

262

263 **5 Shortened equilibrium conditions of HO₂ and OH in the upper mesosphere and lower** 264 **thermosphere**

265 The above analysis revealed, that the reactions describing the equilibrium conditions (7-8) in the
 266 lower and middle mesosphere are different from those in the upper mesosphere and lower thermosphere.
 267 This means that the task of applying these conditions can be divided into two parts depending on the
 268 selected altitude range. At the upper mesosphere and lower thermosphere altitudes, we can consider only
 269 the HO_x – O_x chemistry, excluding the reactions with participation of H₂O₂, N, NO, NO₂, and CO. In
 270 addition, we can omit the reactions $HO_2+O_3 \rightarrow OH+2O_2$, $OH+O_3 \rightarrow O_2+HO_2$, and $OH+HO_2 \rightarrow H_2O+O_2$
 271 due to their insignificance here. As a result, the shortened equilibrium conditions of HO₂ and OH for this
 272 altitude range are as follows:

$$273 \quad HO_{2sh}^{eq} = \frac{k_{20} \cdot H \cdot M \cdot O_2}{k_{18} \cdot O + (k_{14} + k_{15} + k_{16}) \cdot H} \quad (9)$$

$$274 \quad OH_{sh}^{eq} = \frac{k_{21} \cdot H \cdot O_3 + k_{18} \cdot O \cdot HO_2 + 2 \cdot k_{14} \cdot H \cdot HO_2}{k_{17} \cdot O} \quad (10)$$

275 Figure 5 shows height-latitude cross sections for the $\langle HO_2/HO_{2sh}^{eq} \rangle$ ratio for each month. In each
 276 panel the upper longest black line marks the lower boundary of the main equilibrium area, where

277 according to condition (1) $HO_2 \approx HO_{2sh}^{eq}$ with possible bias of less than 10%. As in the case of Figure 1,
 278 this area extends from the top of the analyzed altitude range. There are also very small equilibrium areas
 279 below, which can be omitted from our consideration. The height of the lower boundary of the main
 280 equilibrium area, $z_{HO_{2sh}^{eq}}$, depends essentially on the season and latitude. Comparing with Figure 1 one can
 281 see, that it reproduces many features of $z_{HO_{2sh}^{eq}}$ at low and middle latitudes. In particular, $z_{HO_{2sh}^{eq}}$ varies in
 282 the interval between 73 and 85 km, as in the case of $z_{HO_2^{eq}}$. In the middle latitudes $z_{HO_{2sh}^{eq}}$ in summer is
 283 several km higher than in winter. Near the equator $z_{HO_{2sh}^{eq}}$ demonstrates the weakest annual variations and
 284 varies in the range of 81-83 km. So, one can conclude, that the exclusion of a number of reactions does
 285 not lead to significant changes in the space-time distributions of the HO_2 equilibrium.

286 Figure 6 plots height-latitude cross sections for the $\langle OH/OH_{sh}^{eq} \rangle$ ratio for each month. As in the
 287 previous case, this is the lower boundary of the equilibrium area, where according to condition (1)
 288 $OH \approx OH_{sh}^{eq}$ with good precision. The dependence of the boundary height, $z_{OH_{sh}^{eq}}$, on the season and
 289 latitude mainly repeats the behavior of $z_{HO_{2sh}^{eq}}$. In particular $z_{OH_{sh}^{eq}}$ varies in the interval between 73 and 85
 290 km. At middle latitudes $z_{OH_{sh}^{eq}}$ in summer is several km higher than in winter. Near the equator $z_{OH_{sh}^{eq}}$ also
 291 demonstrates the weakest annual variations and varies in the range of 81-83 km. Nevertheless, in some
 292 cases the OH equilibrium boundary lies slightly higher than the HO_2 boundary. In particular it can be seen
 293 in April-August above 50°S, which can be explained by the difference between HO_2 and OH lifetimes
 294 ($\tau_{HO_2} < \tau_{OH}$), mainly due to $k_{18} > k_{17}$. Comparing with Figure 2, one can see the exclusion of the
 295 mentioned reactions from consideration results in the absence of the OH equilibrium areas at the low and
 296 middle mesosphere altitudes, as expected.

297

298 **6 The criteria for HO_2 and OH equilibrium validity in the upper mesosphere and lower** 299 **thermosphere**

300 Firstly we determine HO_2 and OH lifetimes and the local time scales of HO_{2sh}^{eq} and OH_{sh}^{eq} ,
 301 according to Section 2.

302 From Eqs. (2-3) and (9), HO_2 lifetime and the local time scales of HO_{2sh}^{eq} are as follows:

$$303 \tau_{HO_2} = \frac{1}{k_{18} \cdot O + (k_{14} + k_{15} + k_{16}) \cdot H}, \quad (11)$$

$$304 \tau_{HO_{2sh}^{eq}} = \frac{HO_{2sh}^{eq}}{|dHO_{2sh}^{eq}/dt|}. \quad (12)$$

305 Then we find the expression for dHO_{2sh}^{eq}/dt :

$$306 \quad \frac{dHO_{2sh}^{eq}}{dt} = \frac{k_{18} \cdot k_{20} \cdot M \cdot O_2 \cdot \frac{d}{dt} \left(\frac{H}{O} \right) \cdot O^2}{(k_{18} \cdot O + (k_{14} + k_{15} + k_{16}) \cdot H)^2} = - \frac{k_{18} \cdot k_{20} \cdot M \cdot O_2 \cdot \frac{d}{dt} \left(\frac{O}{H} \right) \cdot H^2}{(k_{18} \cdot O + (k_{14} + k_{15} + k_{16}) \cdot H)^2}. \quad (13)$$

307 Kulikov et al. (2023a) analyzed the local nighttime evolution of O and H within the framework of pure
 308 HO_x – O_x chemistry and found the expression for $\frac{d}{dt} \left(\frac{O}{H} \right)$:

$$309 \quad \frac{d}{dt} \left(\frac{O}{H} \right) = -2 \cdot k_{20} \cdot M \cdot O_2 \cdot \left(1 - \frac{k_{15} + k_{16}}{k_{18}} \right) - k_{21} \cdot O_3 - k_{12} \cdot M \cdot O_2 \cdot \frac{O}{H}. \quad (14)$$

310 Thus, Eq. (13) can be rewritten in the following form:

$$311 \quad \frac{dHO_{2sh}^{eq}}{dt} = \frac{k_{18} \cdot k_{20} \cdot M \cdot O_2 \cdot H^2 \cdot \left(2 \cdot k_{20} \cdot M \cdot O_2 \cdot \left(1 - \frac{k_{15} + k_{16}}{k_{18}} \right) + k_{21} \cdot O_3 + k_{12} \cdot M \cdot O_2 \cdot \frac{O}{H} \right)}{(k_{18} \cdot O + (k_{14} + k_{15} + k_{16}) \cdot H)^2}. \quad (15)$$

312 By combining Eqs. (9), (12), and (15) we obtain the expression for the local time scales of HO_{2sh}^{eq} :

$$313 \quad \tau_{HO_{2sh}^{eq}} = \frac{(k_{18} \cdot O + (k_{14} + k_{15} + k_{16}) \cdot H)}{k_{18} \cdot H \cdot \left(2 \cdot k_{20} \cdot M \cdot O_2 \cdot \left(1 - \frac{k_{15} + k_{16}}{k_{18}} \right) + k_{21} \cdot O_3 + k_{12} \cdot M \cdot O_2 \cdot \frac{O}{H} \right)} \quad (16)$$

314 Thus, taking into account Eqs. (4), (11) and (16), the criterion for HO₂ equilibrium validity is written in
 315 the form:

$$316 \quad Crit_{HO_2} = \frac{\tau_{HO_2}}{\tau_{HO_{2sh}^{eq}}} = \frac{k_{18} \cdot H \cdot \left(2 \cdot k_{20} \cdot M \cdot O_2 \cdot \left(1 - \frac{k_{15} + k_{16}}{k_{18}} \right) + k_{21} \cdot O_3 + k_{12} \cdot M \cdot O_2 \cdot \frac{O}{H} \right)}{(k_{18} \cdot O + (k_{14} + k_{15} + k_{16}) \cdot H)^2} \leq 0.1. \quad (17)$$

317 We calculated $Crit_{HO_2}$, using the global 3D chemical transport model, and included the zonally and
 318 monthly averaged lines $\langle Crit_{HO_2} \rangle = 0.1$ in Figure 5 (see magenta lines). One can see that, depending
 319 on the month, each magenta line reproduces well the lower boundary of the main HO₂ equilibrium area
 320 and follows almost all its features and variations. Note, that in the zeroth order approximation the
 321 criterion (17) can be simplified as

$$322 \quad Crit_{HO_2} \approx \left(2 \cdot k_{20} \cdot M \cdot O_2 \cdot \left(1 - \frac{k_{15} + k_{16}}{k_{18}} \right) + k_{21} \cdot O_3 + k_{12} \cdot M \cdot O_2 \cdot \frac{O}{H} \right) \cdot \frac{H}{k_{18} \cdot O^2} \leq 0.1. \quad (18)$$

323 From Eqs. (2-3) and (10), OH lifetime and the local time scales of OH_{sh}^{eq} are as follows:

$$324 \quad \tau_{OH} = \frac{1}{k_{17} \cdot O}, \quad (19)$$

$$325 \quad \tau_{OH_{sh}^{eq}} = \frac{OH_{sh}^{eq}}{|dOH_{sh}^{eq}/dt|}. \quad (20)$$

326 Before determining the expression for dOH_{sh}^{eq}/dt one should keep in mind, that the expression (10)
 327 depends on the HO₂ concentration. As previously mentioned, near and above the OH equilibrium
 328 boundary HO₂ is in equilibrium ($HO_2 \approx HO_{2sh}^{eq}$) and we can use Eq. (9). In view of $k_{18} \cdot O \gg$
 329 $(k_{14} + k_{15} + k_{16}) \cdot H$,

330 $HO_{2sh}^{eq} \approx \frac{k_{20} \cdot H \cdot M \cdot O_2}{k_{18} \cdot O} \left(1 - \frac{(k_{14} + k_{15} + k_{16}) \cdot H}{k_{18} \cdot O}\right).$ (21)

331 The substitution of Eq. (21) into Eq. (10) yields:

332 $OH_{sh}^{eq} = k_{20} \cdot H \cdot M \cdot O_2 \cdot \frac{(1 + \frac{2 \cdot k_{14} \cdot H}{k_{18} \cdot O}) \cdot (1 - \frac{(k_{14} + k_{15} + k_{16}) \cdot H}{k_{18} \cdot O})}{k_{17} \cdot O} + \frac{k_{21} \cdot H \cdot O_3}{k_{17} \cdot O} \approx \frac{k_{20} \cdot H \cdot M \cdot O_2}{k_{17} \cdot O} \cdot \left(1 + \frac{(k_{14} - k_{15} - k_{16}) \cdot H}{k_{18} \cdot O}\right) +$
 333 $\frac{k_{21} \cdot H \cdot O_3}{k_{17} \cdot O}$ (22)

334 Thus, the expression for dOH_{sh}^{eq}/dt is:

335 $\frac{dOH_{sh}^{eq}}{dt} = \frac{d}{dt} \left(\frac{H}{O}\right) \cdot \left(\frac{k_{20} \cdot M \cdot O_2}{k_{17}} \cdot \left(1 + \frac{2 \cdot (k_{14} - k_{15} - k_{16}) \cdot H}{k_{18} \cdot O}\right) + \frac{k_{21} \cdot O_3}{k_{17}}\right) + \frac{k_{21} \cdot H}{k_{17} \cdot O} \frac{dO_3}{dt}.$ (23)

336 Taking into account Eq. (14) and the differential equation for O_3 time evolution:

337 $\frac{dO_3}{dt} = k_{12} \cdot M \cdot O_2 \cdot O - k_{21} \cdot H \cdot O_3,$

338 the expression (23) can be rewritten in following form:

339 $\frac{dOH_{sh}^{eq}}{dt} = \frac{(2 \cdot k_{20} \cdot M \cdot O_2 \cdot (1 - \frac{k_{15} + k_{16}}{k_{18}}) + k_{21} \cdot O_3 + k_{12} \cdot M \cdot O_2 \cdot \frac{O}{H}) \cdot H^2}{O^2} \cdot \left(\frac{k_{20} \cdot M \cdot O_2}{k_{17}} \cdot \left(1 + \frac{2 \cdot (k_{14} - k_{15} - k_{16}) \cdot H}{k_{18} \cdot O}\right) + \frac{k_{21} \cdot O_3}{k_{17}}\right) +$
 340 $\frac{k_{21} \cdot H \cdot (k_{12} \cdot M \cdot O_2 \cdot O - k_{21} \cdot H \cdot O_3)}{k_{17} \cdot O}.$ (24)

341 Thus, by combining Eqs. (4), (19), (20), (22), and (24) we obtain the expression for the criterion for OH
 342 equilibrium validity:

343 $Crit_{OH} = \frac{\tau_{OH}}{\tau_{OH_{sh}^{eq}}} =$
 344 $\frac{\left(\left(2 \cdot k_{20} \cdot M \cdot O_2 \cdot \left(1 - \frac{k_{15} + k_{16}}{k_{18}}\right) + k_{21} \cdot O_3 \cdot \frac{H}{O} + k_{12} \cdot M \cdot O_2\right) \cdot \left(k_{20} \cdot M \cdot O_2 \cdot \left(1 + \frac{2 \cdot (k_{14} - k_{15} - k_{16}) \cdot H}{k_{18} \cdot O}\right) + k_{21} \cdot O_3\right) + k_{21} \cdot (k_{12} \cdot M \cdot O_2 \cdot O - k_{21} \cdot H \cdot O_3)\right)}{k_{17} \cdot O \cdot \left(k_{20} \cdot M \cdot O_2 \cdot \left(1 + \frac{(k_{14} - k_{15} - k_{16}) \cdot H}{k_{18} \cdot O}\right) + k_{21} \cdot O_3\right)} \leq$
 345 0.1. (25)

346 We calculated $Crit_{OH}$, using the global 3D chemical transport model, and included the zonally and
 347 monthly averaged lines $\langle Crit_{OH} \rangle = 0.1$ in Figure 6 (see magenta lines). One can see that, depending on
 348 the month, the magenta line almost everywhere reproduces the lower boundary of the OH equilibrium
 349 area and repeats mainly its features and variations. Nevertheless, there are a few (by latitude) narrow
 350 areas (in April-August near 70°S and in October-December near 70°N), where the criterion gives a few
 351 km lower position of the OH equilibrium boundary. Our analysis revealed, that the main reason for that is
 352 the lack of $OH + CO \rightarrow H + CO_2$ reaction among the sources of H in the corresponding differential equation
 353 of its chemical balance. In order to improve the criterion we revised the derivation of expression (14) for
 354 $\frac{d}{dt} \left(\frac{O}{H}\right)$ following to Kulikov et al. (2023a):

$$\begin{aligned}
355 \quad \frac{d}{dt} \left(\frac{O}{H} \right) &= -2 \cdot k_{20} \cdot M \cdot O_2 \cdot \left(1 - \frac{k_{15} + k_{16}}{k_{18}} \right) - k_{21} \cdot O_3 - k_{12} \cdot M \cdot O_2 \cdot \frac{O}{H} - \frac{k_{32} \cdot CO}{k_{17} \cdot H} \cdot (k_{20} \cdot M \cdot O_2 \cdot (1 + \\
356 \quad &\frac{(k_{14} - k_{15} - k_{16}) \cdot H}{k_{18} \cdot O}) + k_{21} \cdot O_3)). \tag{26}
\end{aligned}$$

357 As a result the corrected criterion for OH equilibrium validity is as follows:

$$\begin{aligned}
358 \quad Crit_{OH}^m &= \frac{2 \cdot k_{20} \cdot M \cdot O_2 \cdot \left(1 - \frac{k_{15} + k_{16}}{k_{18}} \right) + k_{21} \cdot O_3 + k_{12} \cdot M \cdot O_2 \cdot \frac{O}{H} + \frac{k_{32} \cdot CO}{k_{17} \cdot H} \cdot (k_{20} \cdot M \cdot O_2 \cdot (1 + \frac{(k_{14} - k_{15} - k_{16}) \cdot H}{k_{18} \cdot O}) + k_{21} \cdot O_3))}{k_{17} \cdot O \cdot (k_{20} \cdot M \cdot O_2 \cdot (1 + \frac{(k_{14} - k_{15} - k_{16}) \cdot H}{k_{18} \cdot O}) + k_{21} \cdot O_3)} \cdot \frac{H}{O} \cdot \\
359 \quad &\left(k_{20} \cdot M \cdot O_2 \cdot \left(1 + \frac{2 \cdot (k_{14} - k_{15} - k_{16}) \cdot H}{k_{18} \cdot O} \right) + k_{21} \cdot O_3 \right) + \frac{k_{21} \cdot (k_{12} \cdot M \cdot O_2 \cdot O - k_{21} \cdot H \cdot O_3)}{k_{17} \cdot O \cdot (k_{20} \cdot M \cdot O_2 \cdot (1 + \frac{(k_{14} - k_{15} - k_{16}) \cdot H}{k_{18} \cdot O}) + k_{21} \cdot O_3)} \leq 0.1 \tag{27}
\end{aligned}$$

360 We calculated this criterion, using the global 3D chemical transport model and included the zonally and
361 monthly averaged lines $\langle Crit_{OH}^m \rangle = 0.1$ on the OH equilibrium maps (see Figure 7). One can see that,
362 the inclusion of this additional term actually eliminates the noted discrepancy between OH boundary and
363 criterion. But the application of this criterion requires CO data.

364 Note also, that our numerical analysis shows that in the zeroth order approximation the criterion
365 (25) can be simplified as:

$$366 \quad Crit_{OH} \approx \left(2 \cdot k_{20} \cdot M \cdot O_2 \cdot \left(1 - \frac{k_{15} + k_{16}}{k_{18}} \right) + k_{21} \cdot O_3 + k_{12} \cdot M \cdot O_2 \cdot \frac{O}{H} \right) \cdot \frac{H}{k_{17} \cdot O^2} \leq 0.1. \tag{28}$$

367

368 7 Discussion

369 We now discuss obtained results and their possible applications.

370 Pay attention to the fact, that the presented results were plotted, using the lower threshold at 105° for the
371 nighttime solar zenith angle (χ) to exclude the twilight transition processes. Nevertheless, our additional
372 analysis revealed, that OH and HO₂ equilibrium conditions are fulfilled at $\chi > 95^\circ$ (see Figs. S1-S2 and
373 S25-S26 in Supplement). Evidently, during the processing of the measurement data, taking twilight χ in
374 ($95^\circ, 105^\circ$) range into account extends the latitude range of OH and HO₂ equilibria application and allows
375 us to include a noticeable part of the data into consideration. However, in this case one should check for
376 additional condition (Kulikov et al., 2023a):

$$377 \quad e^{\int_{lt_{bn}}^{lt} \tau_{HO_2}^{-1} dt} \gg 1, e^{\int_{lt_{bn}}^{lt} \tau_{OH}^{-1} dt} \gg 1, \tag{29}$$

378 where τ_{HO_2} and τ_{OH} are the HO₂ and OH lifetimes, determined by Eqs. (11) and (19), lt is local time of
379 data, lt_{bn} is the local time at the beginning of the night. Mind, that at night O and H tend to decrease due
380 to the shutdown of the O_x and HO_x family photochemical sources, so τ_{HO_2} and τ_{OH} increase. Thus,
381 analyzing the measurement data one can apply more stringent conditions:

$$e^{\frac{lt-lt_{bn}}{\tau_{HO_2}}} \gg 1, e^{\frac{lt-lt_{bn}}{\tau_{OH}}} \gg 1. \quad (30)$$

The main results were obtained using a 3D model, where temperature and wind distributions are updated every 24 hours. This excluded the influence of the atmospheric wave motion, in particular, associated with tides, which is one of the main dynamical drivers in the tropical mesopause. We carried out additional modeling with the distributions of the main characteristics, calculated by the Canadian Middle Atmosphere Model for the year 2009 (Scinocca et al., 2008) with a 6-hourly frequency for updating. The analysis of the time-height evolution of OH and HO₂, especially at low latitudes, showed that our criteria reproduce quite well the local variations of the OH and HO₂ equilibrium boundaries in such conditions (see Fig. S27 in Supplement).

We evaluated the sensitivity of the presented HO₂ and OH criteria ($Crit_{HO_2}$ and $Crit_{OH}$) to the uncertainties of characteristics, involved in the expressions (17) and (25). The local heights of the OH and HO₂ equilibrium boundaries ($z_{HO_2}^{crit}$ and z_{OH}^{crit}) according to the criteria are determined as the altitudes, at which $Crit_{HO_2} = 0.1$ and $Crit_{OH} = 0.1$ respectively. We considered the whole dataset of nighttime profiles, obtained by the numerical simulation of a one-year global evolution of mesosphere – lower thermosphere, and estimated total uncertainties to determination of $z_{HO_2}^{crit}$ and z_{OH}^{crit} from each local (in time and space) dataset (profiles of O, H, O₃, M, O₂ and temperature). Following the typical analysis presented, for example in Mlynczak et al. (2013a, 2014), each uncertainty was calculated as a root sum square of the sensitivities to the individual perturbations of certain variables or parameters in the expressions (17) and (25). The following uncertainties of the variables were used: 5K in the temperature and 30% in O₃, O, and H. The uncertainties in reaction rates and their temperature dependencies were taken from Burkholder et al. (2020). As the result (see Figure 8), the monthly and longitudinally mean of total uncertainties in determination of $z_{HO_2}^{crit}$ and z_{OH}^{crit} were found varying in the range 0.02-1 km, depending on altitude and season. Note, that these values are comparable with the typical height resolution of satellite data. The latter allows us to consider our criteria as a robust instrument for equilibrium condition validation. The main reason of relatively low sensitivity of $z_{HO_2}^{crit}$ and z_{OH}^{crit} is the strong height-dependence of $Crit_{HO_2}$ and $Crit_{OH}$ near the value of 0.1 (see Fig. S28 in Supplement).

As noted, Figs. 5-6 represent an interesting peculiarity. At the middle latitudes summer $z_{HO_2}^{eq}$ and z_{OH}^{eq} are remarkably higher than winter ones. For example, in February $z_{HO_2}^{eq}$ at 60°N is ~ 84 km, whereas the one at 60°S is ~ 74 km. Recently, Kulikov et al. (2023b) found such a feature in the evolution of nighttime ozone chemical equilibrium boundary (Fig. 5 there), derived from SABER/TIMED data. The study showed that the boundary closely follows the transition zone that separates strong and weak diurnal oscillations of O and H (see Figs. 1-3 and 13 in Kulikov et al. (2023b)). Above the zone the behavior of

414 components is dynamically driven and seasonality is the result of change in global-scale circulation,
 415 vertical advection being the primary factor according to Wang et al. (2023). In the transition zone and
 416 below O and H concentrations change by orders of magnitude during the night driven by photochemical
 417 processes. Kulikov et al. (2023b) studied the photochemistry at these altitudes and its seasonal
 418 dependence. It was shown analytically that nighttime O decreases with the characteristic time scale
 419 $\tau_O = O/|dO/dt|$ proportional to the O/H value at the beginning of the night (see Eq. (13) there). At the
 420 same time, according to the distributions derived from SABER measurements O/H during summer
 421 daytime (and thus also at the beginning of the night) at the middle latitudes is remarkably less than the
 422 one during winter daytime (see Fig. 14 there). Consequently, summer values of nighttime τ_O below ~ 84
 423 km are significantly shorter than winter ones, so summer O during the night decreases much faster than in
 424 winter. In our case lifetimes of HO_2 and OH are proportional mainly to $\frac{1}{O}$ (see Eqs. (11) and (19)), so,
 425 following the approach described in Section 2, the summer rise of $z_{\text{HO}_2^{eq}}^{sh}$ and $z_{\text{OH}^{eq}}^{sh}$ at the middle
 426 latitudes can be explained by the season difference in O diurnal photochemical evolution at these
 427 altitudes.

428 As noted in the Introduction, the conditions of nighttime OH and HO_2 equilibria together with one
 429 for O_3 equilibrium and their analytical criteria constitute a useful tool for retrieval of these components or
 430 other characteristics (for example, O and H) from measured data. At the altitudes of upper mesosphere –
 431 lower thermosphere these conditions can be applied, for example, to MLS/Aura database (measured
 432 characteristics: OH, HO_2 , O_3 , and CO), SMILES (HO_2 and O_3), SCIAMACHY ($\text{O}(^1\text{S})$ green-line, O_2 A-
 433 band, and OH Meinel band emissions), SABER/TIMED (O_3 , OH Meinel band emissions at $2.0 \mu\text{m}$ ($9 \rightarrow 7$
 434 and $8 \rightarrow 6$ bands) and at $1.6 \mu\text{m}$ ($5 \rightarrow 3$ and $4 \rightarrow 2$ bands)) and other, including improvement of existing
 435 retrieval approaches. In particular, Panka et al. (2021) proposed the method of simultaneous derivation of
 436 O and OH at the levels $v=0-9$ from SABER data (volume emission rates at 2.0 and $1.6 \mu\text{m}$, $VER_{2\mu\text{m}}$ and
 437 $VER_{1.6\mu\text{m}}$) at 80-100 km, taking into account the equilibrium condition for all states of OH. Such
 438 approach is valid for excited states due to their very short lifetimes determined by radiative transitions
 439 and quenching with O_2 , N_2 , and O. In the case of the OH ground state its lifetime is determined by the
 440 reaction $\text{OH} + \text{O} \rightarrow \text{H} + \text{O}_2$ only. It means, that Panka et al. (2021) used an equilibrium condition for total
 441 OH, which, as one can see from Figure 6, may be significantly disrupted above 80 km. On the other hand,
 442 there are latitude ranges and months, when the OH equilibrium boundary drops remarkably below 80 km.
 443 Moreover, the Panka et al. method requires external data about HO_2 , since the reaction $\text{HO}_2 + \text{O} \rightarrow \text{OH} + \text{O}_2$
 444 becomes the important source for OH below 87 km (Panka et al., 2021; see also Figure 4 in our paper).

445 The results of our paper allow modifying the Panka et al. method to extend its capabilities. The
 446 simplest development of this method seems to be the following. First of all, note that the HO_2 equilibrium

447 condition (9) depends on H and O only and can be used within the self-consistent retrieval procedure,
 448 considering the following system of equations:

$$449 \quad OH(v = 1 - 9) = \frac{k_{12} \cdot H \cdot O_3 \cdot M \cdot f(v) + \sum_{v' > v} (a_1(v', v) + a_2(v', v) \cdot O_2 + a_3(v', v) \cdot N_2 + (a_4(v', v) + a_5(v', v)) \cdot O) \cdot OH(v')}{a_6(v) \cdot O + \sum_{v' > v} (a_1(v, v') + a_2(v, v') \cdot O_2 + a_3(v, v') \cdot N_2 + (a_4(v, v') + a_5(v, v')) \cdot O)},$$

$$450 \quad OH(0) = \frac{\sum_{v' > 0} (a_1(v', 0) + a_2(v', 0) \cdot O_2 + a_3(v', 0) \cdot N_2 + (a_4(v', 0) + a_5(v', 0)) \cdot O) \cdot OH(v') + k_{18} \cdot O \cdot HO_2 + 2 \cdot k_{14} \cdot H \cdot HO_2}{k_{17} \cdot O},$$

$$451 \quad HO_2 = \frac{k_{20} \cdot H \cdot M \cdot O_2}{k_{18} \cdot O + (k_{14} + k_{15} + k_{16}) \cdot H},$$

$$452 \quad VER_{2\mu m} = a_1(9, 7) \cdot OH(9) + a_1(8, 9) \cdot OH(8),$$

$$453 \quad VER_{1.6\mu m} = a_1(5, 3) \cdot OH(5) + a_1(4, 2) \cdot OH(4),$$

454 where a_{1-6} are the constant rates of the processes $OH(v) \rightarrow OH(v' < v) + h\nu$, $OH(v) + O_2 \rightarrow OH(v' < v) +$
 455 O_2 , $OH(v) + N_2 \rightarrow OH(v' < v) + N_2$, $OH(v) + O(^3P) \rightarrow OH(v' \leq v-5) + O(^1D)$, $OH(v) + O(^3P) \rightarrow OH(v' < v) +$
 456 $O(^3P)$, and $OH(v) + O(^3P) \rightarrow H + O_2$ respectively. Take into consideration, that this system includes 13
 457 equations with 13 unknown variables. Therefore, the solution to the system for a single set of the SABER
 458 measurements (simultaneously measured profiles of O_3 , T, pressure, $VER_{2\mu m}$, and $VER_{1.6\mu m}$) gives one
 459 simultaneously retrieved profiles of O, H, $OH(v=0-9)$, and HO_2 . By applying the criteria (17) and (25) to
 460 obtained O and H profiles, we verify the fulfillment of OH and HO_2 equilibrium conditions and determine
 461 the height, below which the resulting profiles should be cut. More advanced retrieval procedure would be
 462 statistical, based on Bayesian theorem, taking into account the uncertainties in measurement data and rate
 463 constants. Similarly, for example, to Kulikov et al. (2018a), it should include a derivation of posterior
 464 conditional probability density function of retrieved characteristics and numerical analysis of this
 465 function. Detailed development of this retrieval method is outside of this paper and should be carried out
 466 in a separate work.

467

468 8 Conclusions

469 The presented analysis shows, that there are extended areas in mesosphere and lower thermosphere,
 470 where nighttime HO_2 and OH are close to their local equilibrium concentrations, determined mainly by
 471 the reactions between $HO_x - O_x$ components among themselves and with H_2O_2 , N, NO, NO_2 , and CO. In
 472 upper mesosphere – lower thermosphere the shortened expressions for their local equilibrium
 473 concentrations are valid, including the $HO_x - O_x$ chemistry only. These conditions describe the HO_2 and
 474 OH equilibrium from the top to some lower boundaries, the altitude position of which vary in the interval
 475 between 73 and 85 km and depends essentially on the season and latitude. We proposed analytical
 476 criteria, which almost everywhere reproduces quite well the main features of these boundaries. Due to
 477 weak sensitivity to uncertainties of reaction rates and variables, these criteria can be considered a robust
 478 instrument for HO_2 and OH equilibrium validation. The obtained results allow extending the abilities of

479 the Panka et al. (2021) method to retrieve unmeasured components from SABER data. The simultaneous
480 application of OH and HO₂ equilibrium conditions to the SABER data together with the OH and HO₂
481 criteria to control this equilibrium validity allows us to retrieve all unknown HO_x – O_x components (O, H,
482 OH, and HO₂) and to extend the altitude range of retrieval downward below 80 km and without external
483 information.

484
485 **Data availability.** CMAM data are obtained from the website ([https://climate-](https://climate-modelling.canada.ca/climatemodeldata/cmam/cmam30/)
486 [modelling.canada.ca/climatemodeldata/cmam/cmam30/](https://climate-modelling.canada.ca/climatemodeldata/cmam/cmam30/), last access: 31 July 2024).

487
488 **Code availability.** Code is available upon request.

489
490 **Author contributions.** Conceptualization: MK, MB, AC, SD, AF. Methodology: MK, AF.
491 Investigation: MK, MB, AC, SD. Software: MB, AC. Visualization: MB, AC. Funding Acquisition: MK.
492 Writing – original draft preparation: MK, MB. Writing – review & editing: AC, SD. Supervising: AF.

493
494 **Competing interests.** The authors declare no conflict of interest.

495
496 **Acknowledgements.** The paper is in the memory of Prof. G.M. Fraiman. The authors are grateful to
497 reviewers for providing valuable recommendations to improve the paper.

498
499 **Financial support.** The main results presented in Sects. 3-6 were obtained with the support of the
500 Russian Science Foundation under grant No. 22-12-00064 (<https://rscf.ru/project/22-12-00064/>, last
501 access: 31 July 2024). The analysis in Discussion was carried out at the expense of state assignment No.
502 0729-2020-0037.

503
504 **Supplement link:**

505
506 **References**

507 Avallone, L. M. and Toohey, D. W.: Tests of halogen photochemistry using in situ measurements of ClO
508 and BrO in the lower polar stratosphere, *J. Geophys. Res.*, 106, 10411–1042,
509 <https://doi.org/10.1029/2000JD900831>, 2001.

510 Belikovich, M. V., Kulikov, M. Yu, Grygalashvyly, M., Sonnemann, G. R., Ermakova, T. S., Nechaev,
511 A. A., and Feigin, A. M.: Ozone chemical equilibrium in the extended mesopause under the nighttime
512 conditions, *Adv. Space Res.*, 61, 426–432, <https://doi.org/10.1016/j.asr.2017.10.010>, 2018.

513 Berger, U., and U. von Zahn (1999), Two level structure of the mesopause: A model study, *J. Geophys.*
514 *Res.*, 104, 22,083–22,093.

515 Burkholder, J. B., Sander, S. P., Abbatt, J., Barker, J. R., Cappa, C., Crouse, J. D., Dibble, T. S., Huie,
516 R. E., Kolb, C. E., Kurylo, M. J., Orkin, V. L., Percival, C. J., Wilmouth, D. M., and Wine, P. H.:
517 Chemical Kinetics and Photochemical Data for Use in Atmospheric Studies, Evaluation No. 19, JPL
518 Publication 19-5, Jet Propulsion Laboratory, Pasadena, <http://jpldataeval.jpl.nasa.gov>, 2020.

519 Cantrell, C. A., Mauldin, L., Zondlo, M., Eisele, F., Kosciuch, E., Shetter, R., Lefer, B., Hall, S., Campos,
520 T., Ridley, B., Walega, J., Fried, A., Wert, B., Flocke, F., Weinheimer, A., Hannigan, J., Coffey, M.,
521 Atlas, E., Stephens, S., Heikes, B., Snow, J., Blake, D., Blake, N., Katzenstein, A., Lopez, J., Browell, E.
522 V., Dibb, J., Scheuer, E., Seid, G., and Talbot, R.: Steady state free radical budgets and ozone
523 photochemistry during TOPSE, *J. Geophys. Res.*, 108, TOP9-1–TOP9-22,
524 <https://doi.org/10.1029/2002JD002198>, 2003.

525 Evans, W. F. J., and Llewellyn, E. J.: Atomic hydrogen concentrations in the mesosphere and the
526 hydroxyl emissions, *J. Geophys. Res.*, 78, 323–326, <https://doi.org/10.1029/JA078i001p00323>, 1973.

527 Evans, W. F. J., McDade, I. C., Yuen, J., and Llewellyn, E. J.: A rocket measurement of the O₂ infrared
528 atmospheric (0-0) band emission in the dayglow and a determination of the mesospheric ozone and
529 atomic oxygen densities, *Can. J. Phys.*, 66, 941–946, <https://doi.org/10.1139/p88-151>. 1988.

530 Fytterer, T., von Savigny, C., Mlynczak, M., and Sinnhuber, M.: Model results of OH airglow
531 considering four different wavelength regions to derive night-time atomic oxygen and atomic hydrogen in
532 the mesopause region, *Atmos. Chem. Phys.*, 19, 1835–1851, <https://doi.org/10.5194/acp-19-1835-2019>,
533 2019.

534 Good, R. E.: Determination of atomic oxygen density from rocket borne measurements of hydroxyl
535 airglow, *Planet. Space Sci.*, 24, 389–395, [https://doi.org/10.1016/0032-0633\(76\)90052-0](https://doi.org/10.1016/0032-0633(76)90052-0), 1976.

536 Grygalashvyly, M., Sonnemann, G. R., and Hartogh, P.: Long-term behavior of the concentration of the
537 minor constituents in the mesosphere - a model study, *Atmos. Chem. Phys.*, 9, 2779–2792,
538 <https://doi.org/10.5194/acp-9-2779-2009>, 2009.

539 Grygalashvyly, M., Sonnemann, G. R., Lübken, F.-J., Hartogh, P., and Berger, U.: Hydroxyl layer: Mean
540 state and trends at midlatitudes, *J. Geophys. Res. Atmos.*, 119, 12,391–12,419,
541 <https://doi.org/10.1002/2014JD022094>, 2014.

542 Grygalashvyly, M.: Several notes on the OH* layer, *Ann. Geophys.*, 33, 923-930,
543 <https://doi.org/10.5194/angeo-33-923-2015>, 2015.

544 Hartogh, P., Jarchow, C., Sonnemann, G. R., and Grygalashvyly, M.: On the spatiotemporal behavior of
545 ozone within the upper mesosphere/mesopause region under nearly polar night conditions, *J. Geophys.*
546 *Res.*, 109, D18303, <https://doi.org/10.1029/2004JD004576>, 2004.

547 Hartogh, P., Jarchow, Ch., Sonnemann, G. R., and Grygalashvyly, M.: Ozone distribution in the middle
548 latitude mesosphere as derived from microwave measurements at Lindau (51.66°N, 10.13°E), *J. Geophys.*
549 *Res.*, 116, D04305, <https://doi.org/10.1029/2010JD014393>, 2011.

550 Körner, U., and Sonnemann, G. R.: Global 3D-modeling of water vapor concentration of the
551 mesosphere/mesopause region and implications with respect to the NLC region, *J. Geophys. Res.*, 106,
552 9639–9651, <https://doi.org/10.1029/2000JD900744>, 2001.

553 Kowalewski, S., v. Savigny, C., Palm, M., McDade, I. C., and Notholt, J.: On the impact of the temporal
554 variability of the collisional quenching process on the mesospheric OH emission layer: a study based on
555 SD-WACCM4 and SABER, *Atmos. Chem. Phys.*, 14, 10193-10210, [https://doi.org/10.5194/acp-14-](https://doi.org/10.5194/acp-14-10193-2014)
556 10193-2014, 2014.

557 Kremp, C., Berger, U., Hoffmann, P., Keuer, D., and Sonnemann, G. R.: Seasonal variation of middle
558 latitude wind fields of the mesopause region—A comparison between observation and model calculation,
559 *Geophys. Res. Lett.*, 26, 1279–1282, <https://doi.org/10.1029/1999GL900218>, 1999.

560 Kulikov, M. Y., Feigin, A. M., and Sonnemann, G. R.: Retrieval of the vertical distribution of chemical
561 components in the mesosphere from simultaneous measurements of ozone and hydroxyl distributions,
562 *Radiophys. Quantum Electron.*, 49, 683–691, <https://doi.org/10.1007/s11141-006-0103-4>, 2006.

563 Kulikov, M. Yu., Feigin, A. M., and Sonnemann, G. R.: Retrieval of water vapor profile in the
564 mesosphere from satellite ozone and hydroxyl measurements by the basic dynamic model of mesospheric
565 photochemical system, *Atmos. Chem. Phys.*, 9, 8199–8210, <https://doi.org/10.5194/acp-9-8199-2009>,
566 2009.

567 Kulikov, M. Y., Belikovich, M. V., Grygalashvyly, M., Sonnemann, G. R., Ermakova, T. S., Nechaev, A.
568 A., and Feigin, A. M.: Daytime ozone loss term in the mesopause region, *Ann. Geophys.*, 35, 677-682
569 <https://doi.org/10.5194/angeo-35-677-2017>, 2017.

570 Kulikov, M. Y., Nechaev, A. A., Belikovich, M. V., Ermakova, T. S., and Feigin, A. M.: Technical note:
571 Evaluation of the simultaneous measurements of mesospheric OH, HO₂, and O₃ under a photochemical
572 equilibrium assumption – a statistical approach, *Atm. Chem. Phys.*, 18, 7453-747,
573 <https://doi.org/10.5194/acp-18-7453-2018>, 2018a.

574 Kulikov, M. Y., Belikovich, M. V., Grygalashvyly, M., Sonnemann, G. R., Ermakova, T. S., Nechaev, A.
575 A., and Feigin, A. M.: Nighttime ozone chemical equilibrium in the mesopause region. *J. Geophys.*
576 *Res.*, 123, 3228–3242, <https://doi.org/10.1002/2017JD026717>, 2018b.

577 Kulikov, M. Yu., Nechaev, A. A., Belikovich, M. V., Vorobeva, E. V., Grygalashvyly, M., Sonnemann,
578 G. R., and Feigin, A. M.: Border of nighttime ozone chemical equilibrium in the mesopause region from
579 SABER data: implications for derivation of atomic oxygen and atomic hydrogen, *Geophys. Res. Lett.*, 46,
580 997–1004, <https://doi.org/10.1029/2018GL080364>, 2019.

581 Kulikov, M. Y., Belikovich, M. V., Feigin, A. M.: The 2-day photochemical oscillations in the mesopause
582 region: the first experimental evidence? *Geophys. Res. Lett.*, 48, e2021GL092795,
583 <https://doi.org/10.1029/2021GL092795>, 2021.

584 Kulikov M.Yu., Belikovich, M.V., Grygalashvyly, M., Sonnemann, G. R., and Feigin, A.M.: Retrieving
585 daytime distributions of O, H, OH, HO₂, and chemical heating rate in the mesopause region from satellite
586 observations of ozone and OH* volume emission: The evaluation of the importance of the reaction
587 $H+O_3\rightarrow O_2+OH$ in the ozone balance, *Adv. Space Res.*, 69(9), 3362-3373,
588 <https://doi.org/10.1016/j.asr.2022.02.011>, 2022a.

589 Kulikov, M. Y., Belikovich, M. V., Grygalashvyly, M., Sonnemann, G. R., and Feigin, A.M.: The revised
590 method for retrieving daytime distributions of atomic oxygen and odd-hydrogens in the mesopause region
591 from satellite observations, *Earth, Planets and Space*, 74, 44, [https://doi.org/10.1186/s40623-022-01603-](https://doi.org/10.1186/s40623-022-01603-8)
592 8, 2022b.

593 Kulikov, M. Yu., Belikovich, M. V., Chubarov, A. G., Dementeyva, S. O., Feigin, A. M.: Boundary of
594 nighttime ozone chemical equilibrium in the mesopause region: improved criterion of determining the
595 boundary from satellite data, *Adv. Space Res.*, 71 (6), 2770-2780,
596 <https://doi.org/10.1016/j.asr.2022.11.005>, 2023a.

597 Kulikov, M. Yu., Belikovich, M. V., Chubarov, A. G., Dementyeva, S. O., and Feigin, A. M.: Boundary
598 of nighttime ozone chemical equilibrium in the mesopause region: long-term evolution determined using
599 20-year satellite observations, *Atmos. Chem. Phys.*, 23, 14593–14608, [https://doi.org/10.5194/acp-23-](https://doi.org/10.5194/acp-23-14593-2023)
600 14593-2023, 2023b.

601 Llewellyn, E. J., McDade, I. C. Moorhouse, P. and Lockertie M. D.: Possible reference models for
602 atomic oxygen in the terrestrial atmosphere, *Adv. Space Res.*, 13, 135–144, [https://doi.org/10.1016/0273-](https://doi.org/10.1016/0273-1177(93)90013-2)
603 1177(93)90013-2, 1993.

604 Llewellyn, E. J., and McDade, I. C.: A reference model for atomic oxygen in the terrestrial atmosphere,
605 *Adv. Space Res.*, 18, 209–226, [https://doi.org/10.1016/0273-1177\(96\)00059-2](https://doi.org/10.1016/0273-1177(96)00059-2), 1996.

606 Manney, G. L., Kruger, K., Sabutis, J. L., Sena, S. A., and Pawson, S.: The remarkable 2003–2004 winter
607 and other recent warm winters in the Arctic stratosphere since the late 1990s. *J. Geophys. Res.*, 110,
608 D04107, <https://doi.org/10.1029/2004JD005367>, 2005.

609 Marchand, M., Bekki, S., Lefevre, F., and Hauchecorne, A.: Temperature retrieval from stratospheric O₃
610 and NO₃ GOMOS data, *Geophys. Res. Lett.*, 34, L24809, <https://doi.org/10.1029/2007GL030280>, 2007.

611 Marsh, D. R., Smith, A. K., Mlynczak, M. G., and Russell III, J. M.: SABER observations of the OH
612 Meinel airglow variability near the mesopause, *J. Geophys. Res.*, 111, A10S05,
613 <https://doi.org/10.1029/2005JA011451>, 2006.

614 McDade, I. C., Llewellyn, E. J., and Harris, F. R.: Atomic oxygen concentrations in the lower auroral
615 thermosphere, *Adv. Space Res.*, 5, 229–232, <https://doi.org/10.1029/GL011I003P00247>, 1985.

616 McDade, I. C., and Llewellyn, E. J.: Mesospheric oxygen atom densities inferred from night-time OH
617 Meinel band emission rates, *Planet. Space Sci.*, 36, 897–905, [https://doi.org/10.1016/0032-
618 0633\(88\)90097-9](https://doi.org/10.1016/0032-0633(88)90097-9), 1988.

619 Mlynczak, M. G., Marshall, B. T., Martin-Torres, F. J., Russell III, J. M., Thompson, R. E., Remsberg, E.
620 E., and Gordley, L. L.: Sounding of the Atmosphere using Broadband Emission Radiometry observations
621 of daytime mesospheric O₂(¹D) 1.27 μm emission and derivation of ozone, atomic oxygen, and solar and
622 chemical energy deposition rates, *J. Geophys. Res.*, 112, D15306, <https://doi.org/10.1029/2006JD008355>,
623 2007.

624 Mlynczak, M. G., Hunt, L. A., Mast, J. C., Marshall, B. T., Russell III, J. M., Smith, A. K., Siskind, D. E.,
625 Yee, J.-H., Mertens, C. J., Martin-Torres, F. J., Thompson, R. E., Drob, D. P., and Gordley, L. L.: Atomic
626 oxygen in the mesosphere and lower thermosphere derived from SABER: Algorithm theoretical basis and
627 measurement uncertainty, *J. Geophys. Res.*, 118, 5724–5735, <https://doi.org/10.1002/jgrd.50401>, 2013a.

628 Mlynczak, M. G., Hunt, L. H., Mertens, C. J., Marshall, B. T., Russell III, J. M., López-Puertas, M.,
629 Smith, A. K., Siskind, D. E., Mast, J. C., Thompson, R. E., and Gordley, L. L.: Radiative and energetic
630 constraints on the global annual mean atomic oxygen concentration in the mesopause region, *J. Geophys.*
631 *Res. Atmos.*, 118, 5796–5802, <https://doi.org/10.1002/jgrd.50400>, 2013b.

632 Mlynczak, M. G., Hunt, L. A. Marshall, B. T. Mertens, C. J. Marsh, D. R. Smith, A. K. Russell, J. M.
633 Siskind D. E., and Gordley L. L.: Atomic hydrogen in the mesopause region derived from SABER:
634 Algorithm theoretical basis, measurement uncertainty, and results, *J. Geophys. Res.*, 119, 3516–3526,
635 <https://doi.org/10.1002/2013JD021263>, 2014.

636 Mlynczak, M. G., Hunt, L. A., Russell, J. M. III, and Marshall, B. T.: Updated SABER night atomic
637 oxygen and implications for SABER ozone and atomic hydrogen, *Geophys. Res. Lett.*, 45, 5735–5741,
638 <https://doi.org/10.1029/2018GL077377>, 2018.

639 Morton, K. W., and Mayers, D. F.; *Numerical Solution of Partial Differential Equations*, Cambridge
640 University Press, 1994.

641 Nikoukar, R., Swenson, G. R., Liu, A. Z., and Kamalabadi, F.: On the variability of mesospheric OH
642 emission profiles, *J. Geophys. Res.*, 112, D19109, <https://doi.org/10.1029/2007JD008601>, 2007.

643 Panka, P. A., Kutepov, A. A., Zhu, Y., Kaufmann, M., Kalogerakis, K. S., Rezac, L., et al.: Simultaneous
644 retrievals of nighttime O(³P) and total OH densities from satellite observations of Meinel band emissions.
645 *Geoph. Res.Lett.*, 48, e2020GL091053, <https://doi.org/10.1029/2020GL091053>, 2021.

646 Pendleton, W. R., Baker, K. D., Howlett, L. C.: Rocket-based investigations of $O(^3P)$, $O_2(a^1\Delta_g)$ and OH^*
647 ($v=1,2$) during the solar eclipse of 26 February 1979, *J. Atm. Terr. Phys.*, 45(7), 479-491, 1983.

648 Siskind, D. E., Marsh, D. R., Mlynczak, M. G., Martin-Torres, F. J., and Russell III, J. M.: Decreases in
649 atomic hydrogen over the summer pole: Evidence for dehydration from polar mesospheric clouds?
650 *Geophys. Res. Lett.*, 35, L13809, <https://doi.org/10.1029/2008GL033742>, 2008.

651 Russell, J. P., and Lowe, R. P.: Atomic oxygen profiles (80-94 km) derived from Wind Imaging
652 Interferometer/Upper Atmospheric Research Satellite measurements of the hydroxyl airglow: 1.
653 Validation of technique, *J. Geophys. Res.*, 108(D21), 4662, <https://doi.org/10.1029/2003JD003454>, 2003.

654 Russell, J. P., Ward, W. E., Lowe, R. P., Roble, R. G., Shepherd, G. G., and Solheim, B.: Atomic oxygen
655 profiles (80 to 115 km) derived from Wind Imaging Interferometer/Upper Atmospheric Research Satellite
656 measurements of the hydroxyl and green line airglow: Local time–latitude dependence, *J. Geophys. Res.*,
657 110(D15), D15305, <https://doi.org/10.1029/2004JD005570>, 2005.

658 Siskind, D. E., Mlynczak, M. G., Marshall, T., Friedrich, M., Gumbel, J.: Implications of odd oxygen
659 observations by the TIMED/SABER instrument for lower D region ionospheric modeling, *J. Atmos. Sol.
660 Terr. Phys.*, 124, 63–70, <https://doi.org/10.1016/j.jastp.2015.01.014>, 2015.

661 Smith, A. K., Lopez-Puertas, M., Garcia-Comas, M. and Tukiainen, S.: SABER observations of
662 mesospheric ozone during NH late winter 2002–2009, *Geophys. Res. Lett.*, 36, L23804,
663 <https://doi.org/10.1029/2009GL040942>, 2009.

664 Smith, A. K., Marsh, D. R. Mlynczak, M. G. and Mast, J. C.: Temporal variations of atomic oxygen in the
665 upper mesosphere from SABER, *J. Geophys. Res.*, 115, D18309, <https://doi.org/10.1029/2009JD013434>,
666 2010.

667 Scinocca, J. F., McFarlane, N. A., Lazare, M., Li, J., and Plummer, D.: The CCCma third generation
668 AGCM and its extension into the middle atmosphere, *Atmos. Chem. Phys.*, 8, 7055–7074,
669 <https://doi.org/10.5194/acp-8-7055-2008>, 2008.

670 Sonnemann, G., Kremp, C. Ebel, A. and Berger U.: A three-dimensional dynamic model of minor
671 constituents of the mesosphere, *Atmos. Environ.*, 32, 3157–3172, [https://doi.org/10.1016/S1352-
672 2310\(98\)00113-7](https://doi.org/10.1016/S1352-2310(98)00113-7), 1998.

673 Sonnemann, G. R., Grygalashvyly, M., Hartogh, P., and Jarchow, C.: Behavior of mesospheric ozone
674 under nearly polar night conditions, *Adv. Space Res.*, 38, 2402–2407,
675 <https://doi.org/10.1016/j.asr.2006.09.011>, 2006.

676 Sonnemann, G. R., Hartogh, P., Grygalashvyly, M., Li, S., and Berger, U.: The quasi 5-day signal in the
677 mesospheric water vapor concentration at high latitudes in 2003—a comparison between observations at
678 ALOMAR and calculations, *J. Geophys. Res.*, 113, D04101, <https://doi.org/10.1029/2007JD008875>,
679 2008.

680 Sonnemann, G. R., Hartogh, P., Berger, U., and Grygalashvyly, M.: Hydroxyl layer: trend of number
681 density and intra-annual variability, *Ann. Geophys.*, 33, 749–767, [https://doi.org/10.5194/angeo-33-749-](https://doi.org/10.5194/angeo-33-749-2015)
682 2015, 2015.

683 Stedman, D. H., Chameides, W., and Jackson, J. O.: Comparison of experimental and computed values
684 for J(NO₂), *Geophys. Res. Lett.*, 2, 22–25, <https://doi.org/10.1029/GL002i001p00022>, 1975.

685 Swenson, G. R., and Gardner C. S.: Analytical models for the responses of the mesospheric OH* and Na
686 layers to atmospheric gravity waves, *J. Geophys. Res.*, 103(D6), 6271–6294,
687 <https://doi.org/10.1029/97JD02985>, 1998.

688 Thomas, R. J.: Atomic hydrogen and atomic oxygen density in the mesosphere region: Global and
689 seasonal variations deduced from Solar Mesosphere Explorer near-infrared emissions, *J. Geophys. Res.*,
690 95, 16,457–16,476, <https://doi.org/10.1029/JD095iD10p16457>, 1990.

691 Walcek, C. J.: Minor flux adjustment near mixing ratio extremes for simplified yet highly accurate
692 monotonic calculation of tracer advection, *J. Geophys. Res.*, 105, 9335–9348,
693 <https://doi.org/10.1029/1999JD901142>, 2000.

694 Wang, J. C., Yue, J., Wang, W., Qian, L., Jones, M., Jr., and Wang, N.: The lower thermospheric winter-
695 to-summer meridional circulation: 2. Impact on atomic oxygen *J. Geophys. Res. Space Phys.*, 128,
696 e2023JA031684, <https://doi.org/10.1029/2023JA031684>, 2023.

697 Xu, J., Smith, A. K., Jiang, G., Gao, H., Wei, Y., Mlynchak, M. G., and Russell III, J. M.: Strong
698 longitudinal variations in the OH nightglow, *Geophys. Res. Lett.*, 37, L21801,
699 <https://doi.org/10.1029/2010GL043972>, 2010.

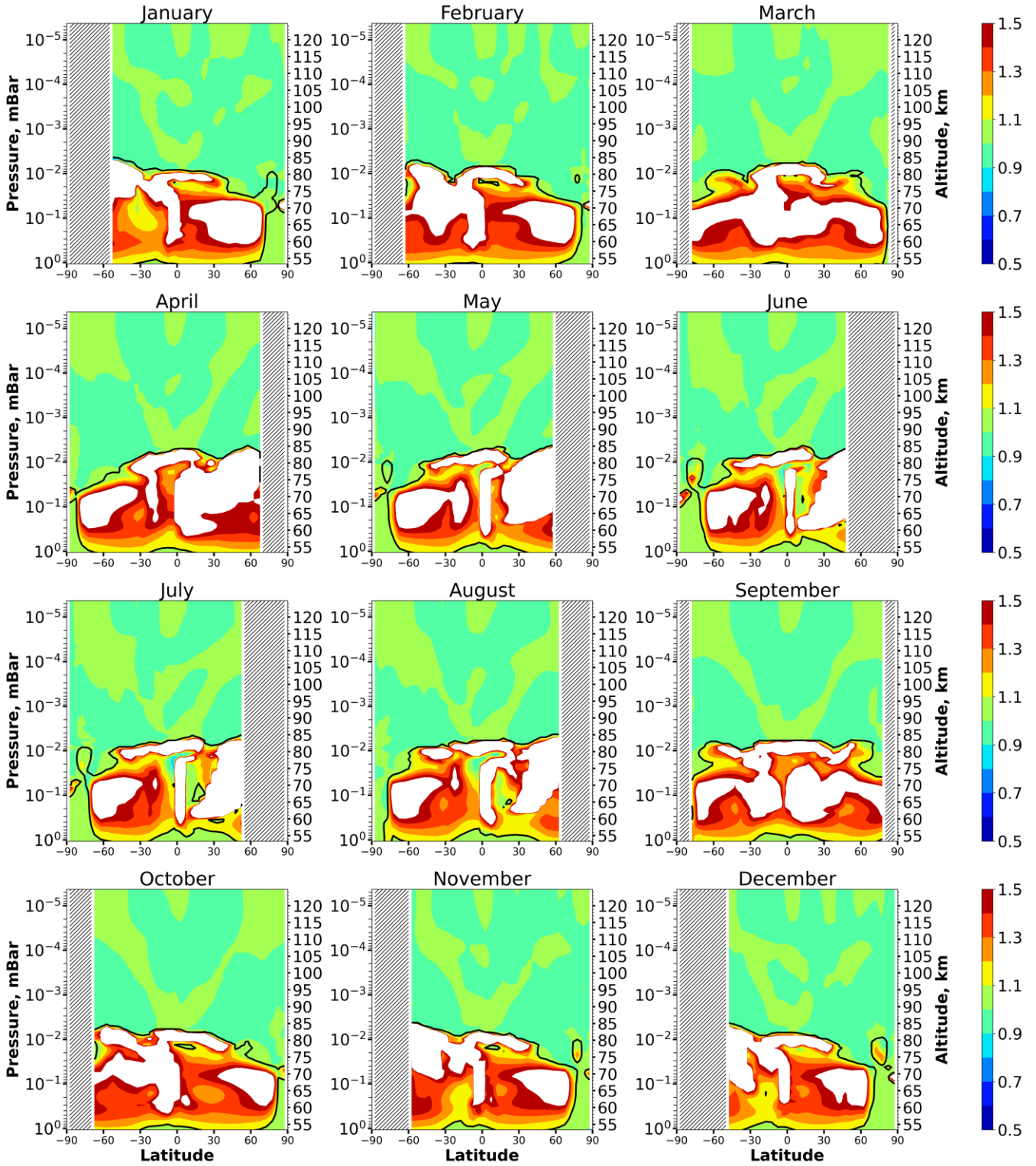
700 Xu, J., Gao, H. Smith, A. K. and Zhu Y.: Using TIMED/SABER nightglow observations to investigate
701 hydroxyl emission mechanisms in the mesopause region, *J. Geophys. Res.*, 117, D02301,
702 <https://doi.org/10.1029/2011JD016342>, 2012.

703 **Table 1.** List of reactions included in 3-d chemical transport model with the corresponding reaction rates
 704 taken from Burkholder et al. (2020).

1	$O(^1D)+O_2 \rightarrow O+O_2$	24	$H+OH+N_2 \rightarrow H_2O+N_2$	47	$NO+O_3 \rightarrow NO_2+O_2$
2	$O(^1D)+N_2 \rightarrow O+N_2$	25	$OH+H_2 \rightarrow H_2O+H$	48	$NO_2+O_3 \rightarrow NO_3+O_2$
3	$O(^1D)+O_3 \rightarrow O_2+2O$	26	$OH+OH \rightarrow H_2O+O$	49	$N+OH \rightarrow NO+H$
4	$O(^1D)+O_3 \rightarrow 2O_2$	27	$OH+OH+M \rightarrow H_2O_2+M$	50	$NO+HO_2 \rightarrow NO_2+OH$
5	$O(^1D)+N_2O \rightarrow 2NO$	28	$OH+HO_2 \rightarrow H_2O+O_2$	51	$H+NO_2 \rightarrow OH+NO$
6	$O(^1D)+N_2O \rightarrow N_2+O_2$	29	$H_2O_2+OH \rightarrow H_2O+HO_2$	52	$NO_3+NO \rightarrow 2NO_2$
7	$O(^1D)+H_2O \rightarrow 2OH$	30	$HO_2+HO_2 \rightarrow H_2O_2+O_2$	53	$N+NO \rightarrow N_2+O$
8	$O(^1D)+H_2 \rightarrow H+OH$	31	$HO_2+HO_2+M \rightarrow H_2O_2+O_2+M$	54	$N+NO_2 \rightarrow N_2O+O$
9	$O(^1D)+CH_4 \rightarrow CH_3+OH$	32	$OH+CO \rightarrow H+CO_2$	55	$O_2+h\nu \rightarrow 2O$
10	$O(^1D)+CH_4 \rightarrow H_2+CH_2O$	33	$CH_4+OH \rightarrow CH_3+H_2O$	56	$O_2+h\nu \rightarrow O+O(^1D)$
11	$O+O+M \rightarrow O_2+M$	34	$CH_3+O_2 \rightarrow CH_3O_2$	57	$O_3+h\nu \rightarrow O_2+O$
12	$O+O_2+M \rightarrow O_3+M$	35	$CH_3+O \rightarrow CH_2O+H$	58	$O_3+h\nu \rightarrow O_2+O(^1D)$
13	$O+O_3 \rightarrow O_2+O_2$	36	$CH_3O_2+NO \rightarrow CH_3O+NO_2$	59	$N_2+h\nu \rightarrow 2N$
14	$H+HO_2 \rightarrow 2OH$	37	$CH_3O+O_2 \rightarrow CH_2O+HO_2$	60	$NO+h\nu \rightarrow N+O$
15	$H+HO_2 \rightarrow H_2O+O$	38	$CH_2O \rightarrow H_2+CO$	61	$NO_2+h\nu \rightarrow NO+O$
16	$H+HO_2 \rightarrow H_2+O_2$	39	$CH_2O \rightarrow H+CHO$	62	$N_2O+h\nu \rightarrow N_2+O(^1D)$
17	$OH+O \rightarrow H+O_2$	40	$CHO+O_2 \rightarrow HO_2+CO$	63	$N_2O+h\nu \rightarrow N+NO$
18	$HO_2+O \rightarrow OH+O_2$	41	$O_3+N \rightarrow NO+O_2$	64	$NO_3+h\nu \rightarrow NO_2+O$
19	$H_2O_2+O \rightarrow OH+HO_2$	42	$NO_3+O \rightarrow NO_2+O_2$	65	$H_2O+h\nu \rightarrow H+OH$
20	$H+O_2+M \rightarrow HO_2+M$	43	$O+NO+M \rightarrow NO_2+M$	66	$H_2O_2+h\nu \rightarrow 2OH$
21	$H+O_3 \rightarrow OH+O_2$	44	$NO_2+O \rightarrow NO+O_2$	67	$CH_4+h\nu \rightarrow CH_2+H_2$
22	$OH+O_3 \rightarrow O_2+HO_2$	45	$NO_2+O+M \rightarrow NO_3+M$	68	$CH_4+h\nu \rightarrow CH+H_2+H$
23	$HO_2+O_3 \rightarrow OH+2O_2$	46	$N+O_2 \rightarrow NO+O$	69	$CO_2+h\nu \rightarrow CO+O$

705

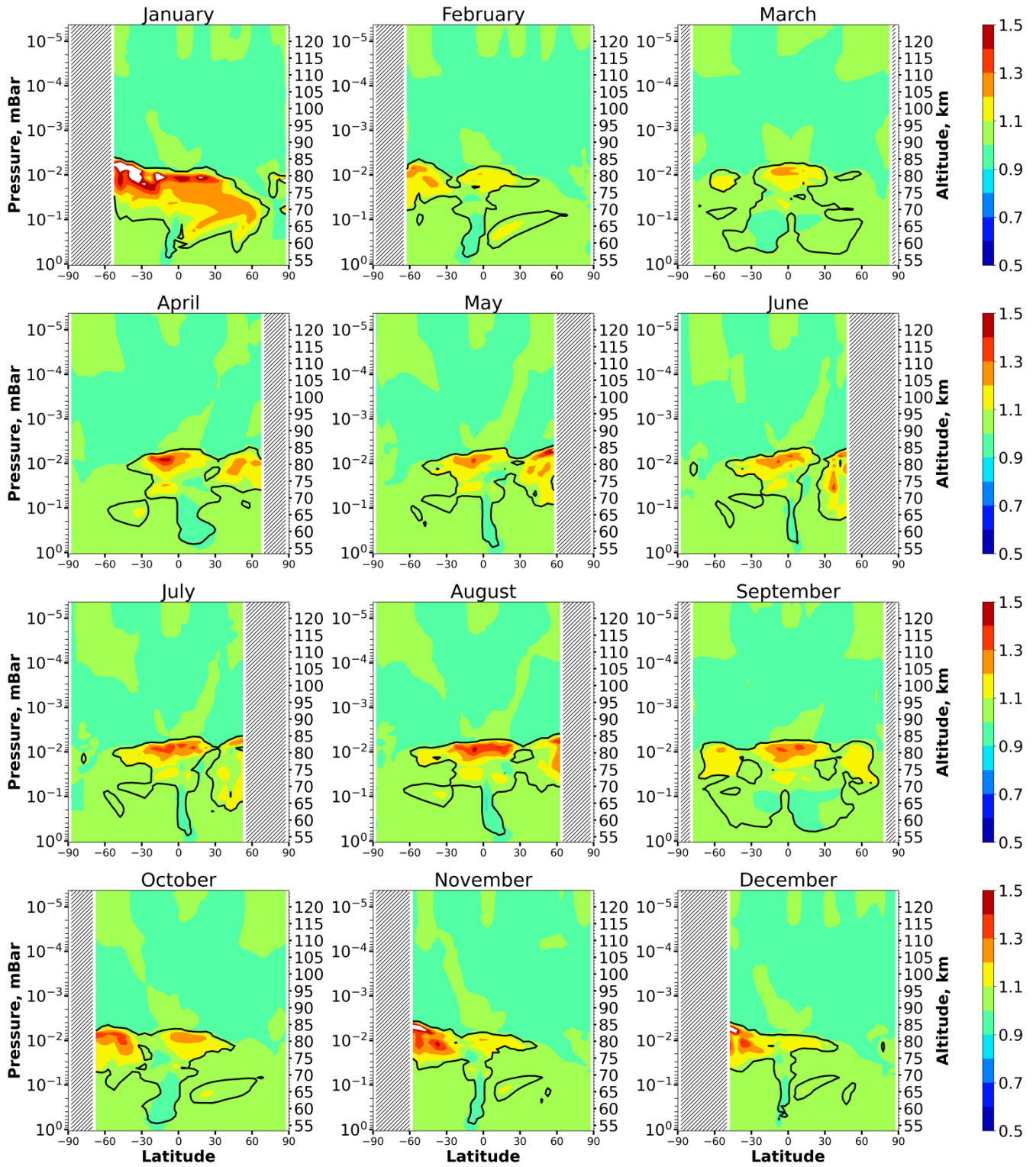
706



707

708 Figure 1. Nighttime mean and monthly averaged HO_2/HO_2^{eq} , where HO_2^{eq} is equilibrium concentration
 709 determined by Eq. (5). Black line shows the boundary of HO_2 equilibrium according to condition (1). The
 710 stippling corresponds to $\chi < 105^\circ$. The white area represents the $\langle HO_2/HO_2^{eq} \rangle$ ratio outside the [0.5,
 711 1.5] interval.

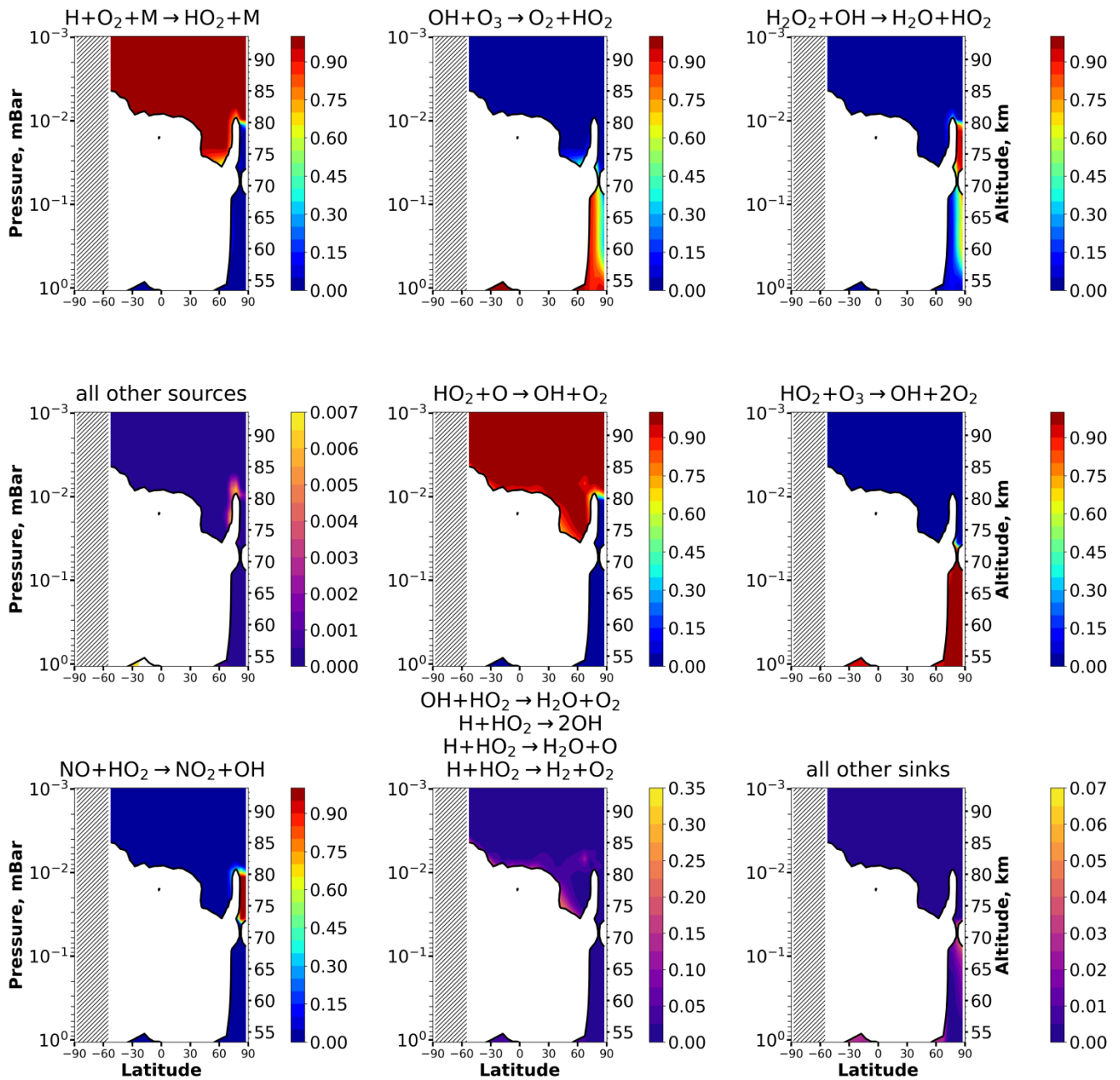
712



713

714 Figure 2. Nighttime mean and monthly averaged OH/OH^{eq} , where OH^{eq} is equilibrium concentration
 715 determined by Eq. (6). Black line shows the boundary of OH equilibrium according to condition (1). The
 716 stippling corresponds to $\chi < 105^\circ$. The white area represents the $\langle OH/OH^{eq} \rangle$ ratio outside the [0.5, 1.5]
 717 interval.

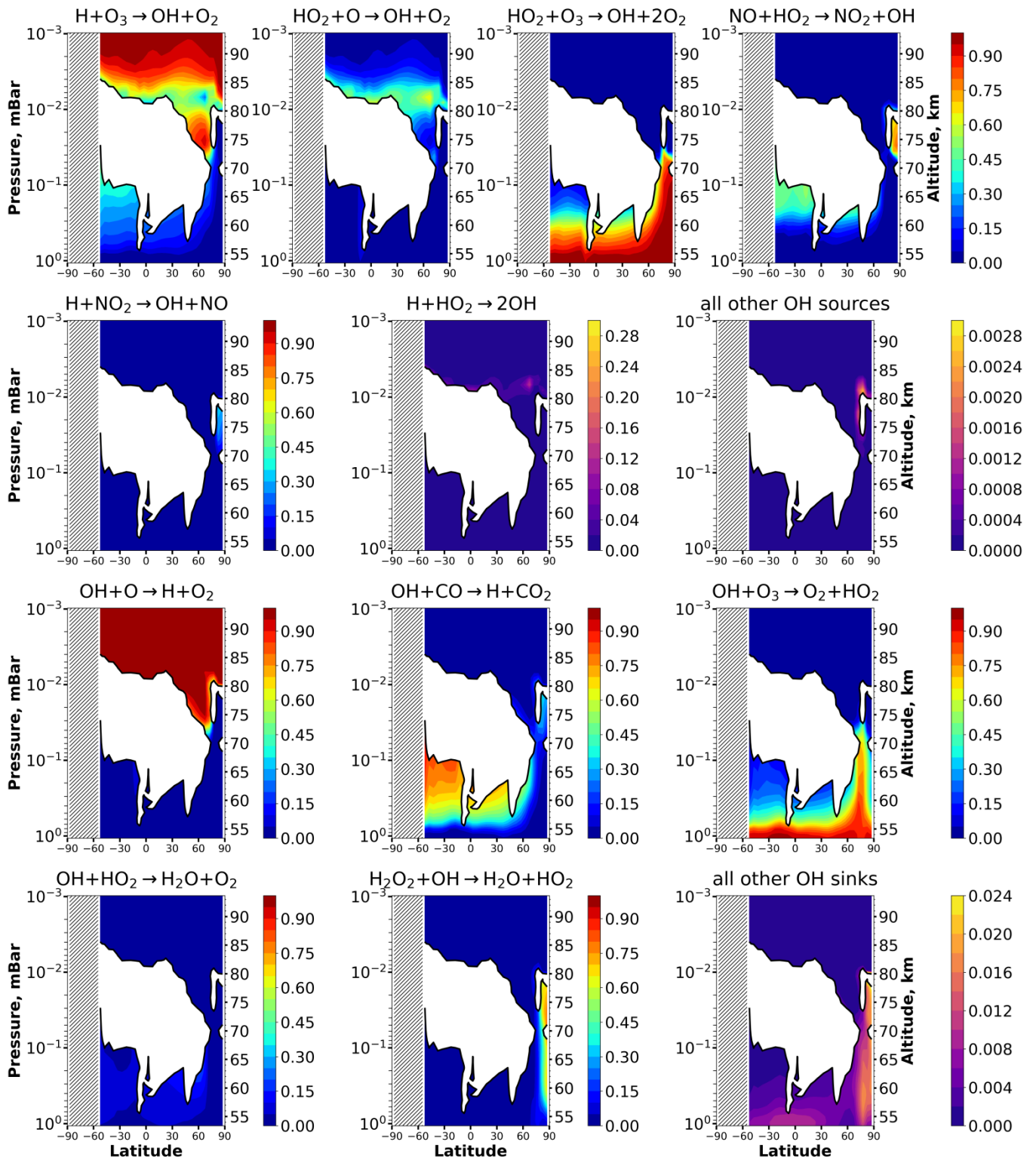
718



719

720 Figure 3. Nighttime mean and monthly averaged relative contribution of a certain reaction to the total
 721 source or sink of HO₂ in equilibrium areas. The stippling corresponds to $\chi < 105^\circ$. White color indicates
 722 nonequilibrium areas of HO₂.

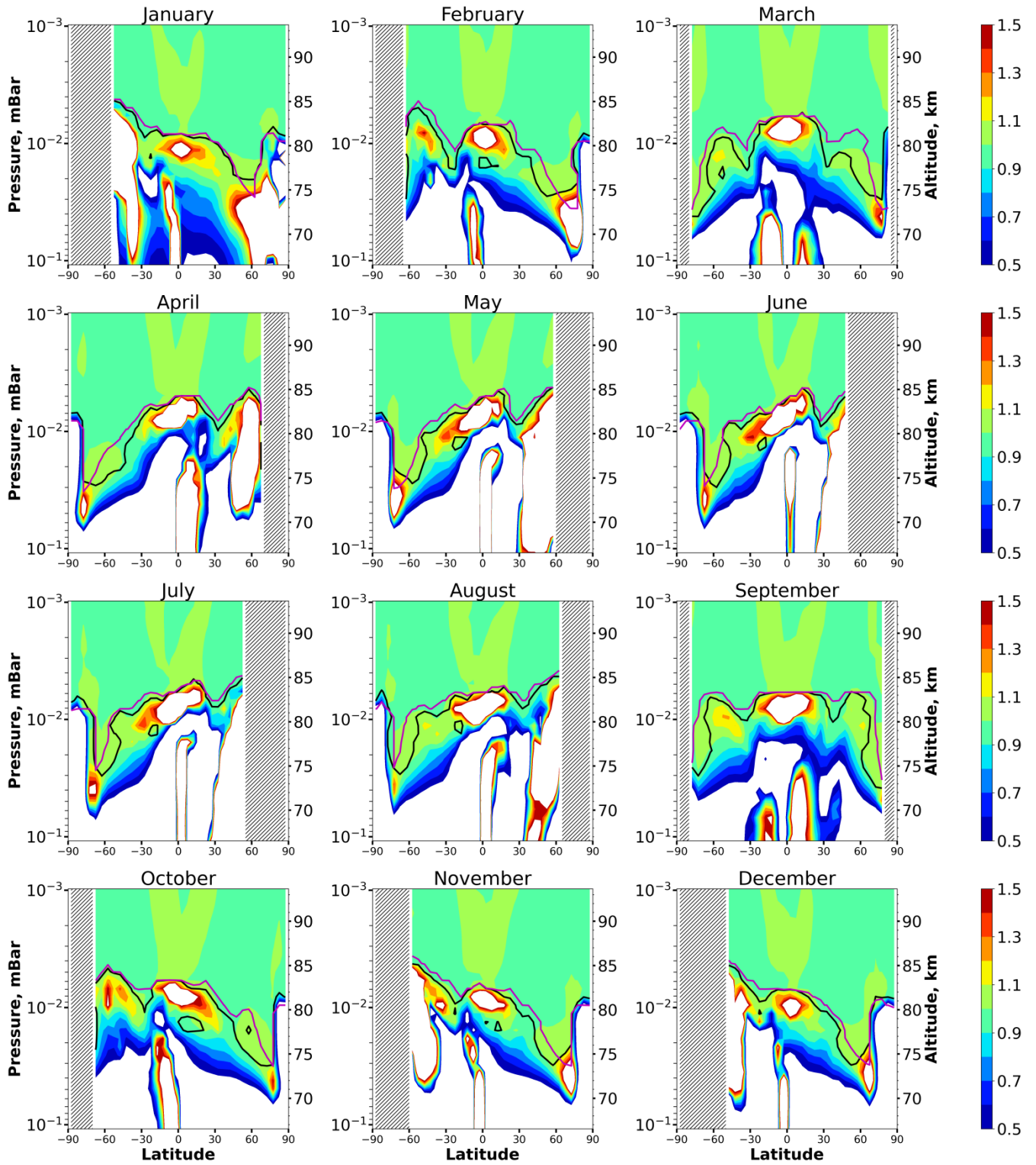
723



724

725 Figure 4. Nighttime mean and monthly averaged relative contribution of a certain reaction to the total
 726 source or sink of OH in equilibrium areas. The stippling corresponds to $\chi < 105^\circ$. White color indicates
 727 nonequilibrium areas of OH.

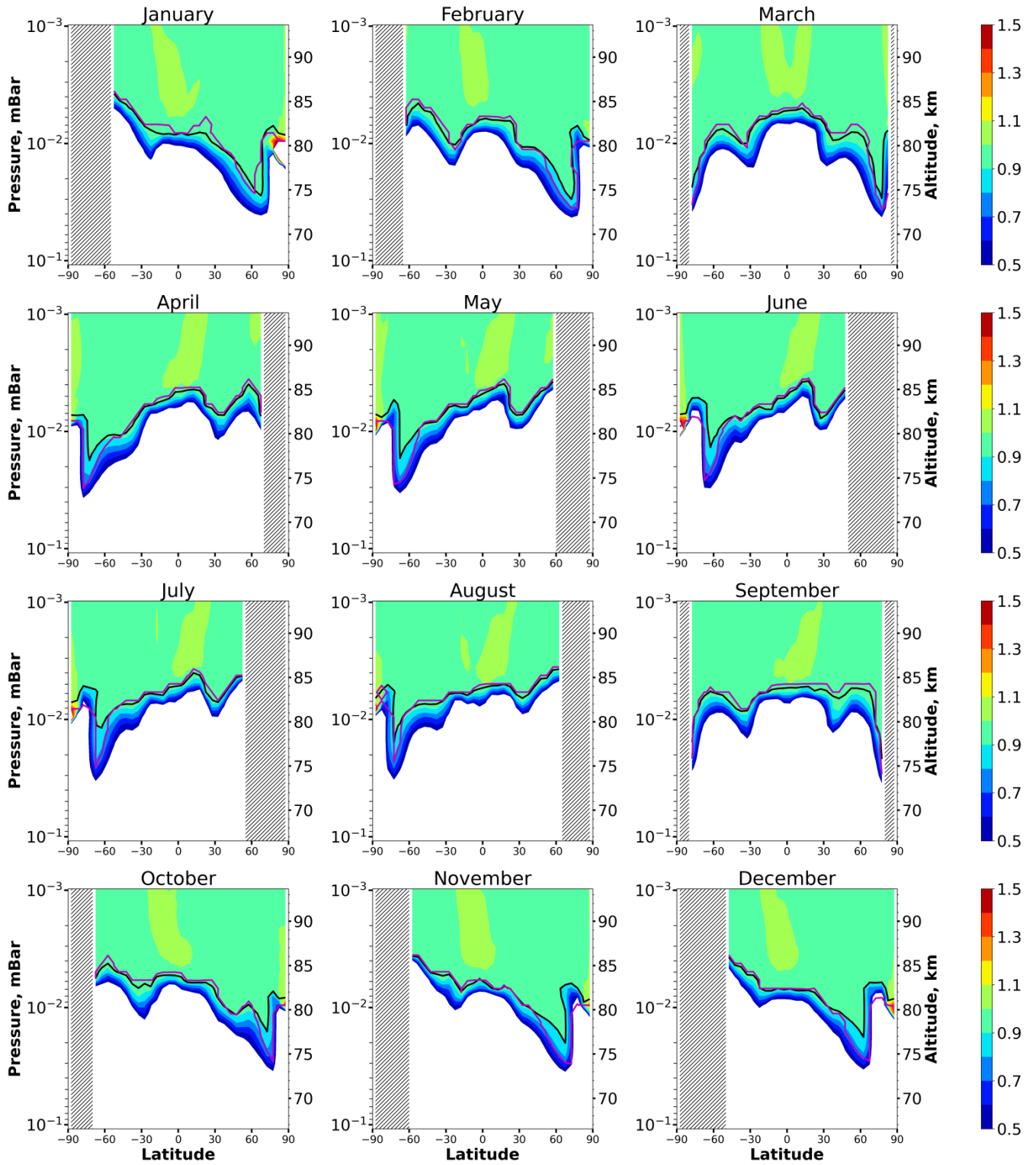
728



729

730 Figure 5. Nighttime mean and monthly averaged HO_2/HO_{2sh}^{eq} , where HO_{2sh}^{eq} is shortened equilibrium
 731 concentration determined by Eq. (9). Black line shows the boundary of HO_2 equilibrium according to
 732 condition (1). Magenta line shows $\langle Crit_{HO_2} \rangle = 0.1$. The stippling corresponds to $\chi < 105^\circ$. The white
 733 area represents the $\langle HO_2/HO_2^{eq} \rangle$ ratio outside the $[0.5, 1.5]$ interval.

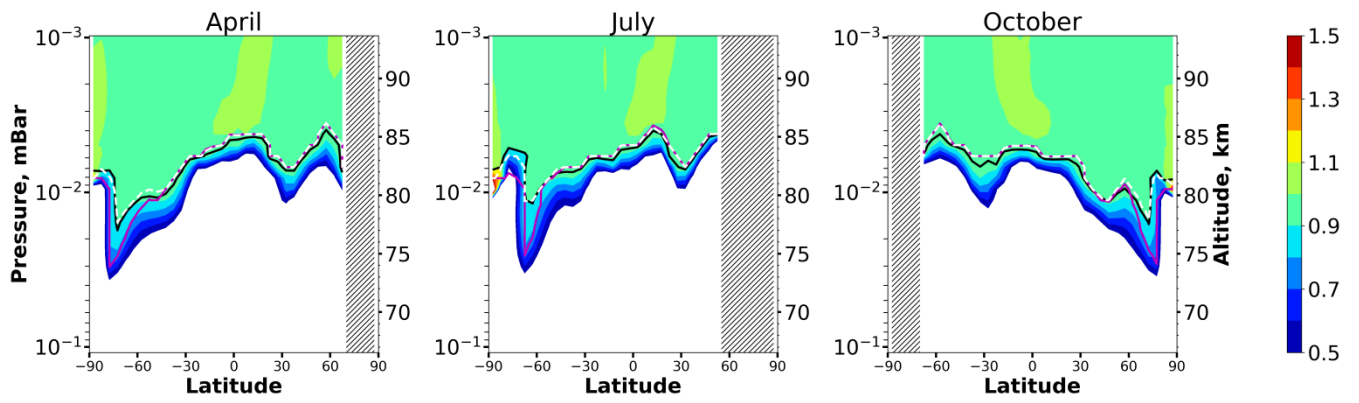
734



735

736 Figure 6. Nighttime mean and monthly averaged OH/OH_{sh}^{eq} , where OH_{sh}^{eq} is shortened equilibrium
 737 concentration determined by Eq. (10). Black line shows the boundary of OH equilibrium according to
 738 condition (1). Magenta line shows $\langle Crit_{OH} \rangle = 0.1$. The stippling corresponds to $\chi < 105^\circ$. The white
 739 area represents the $\langle OH/OH^{eq} \rangle$ ratio outside the $[0.5, 1.5]$ interval.

740

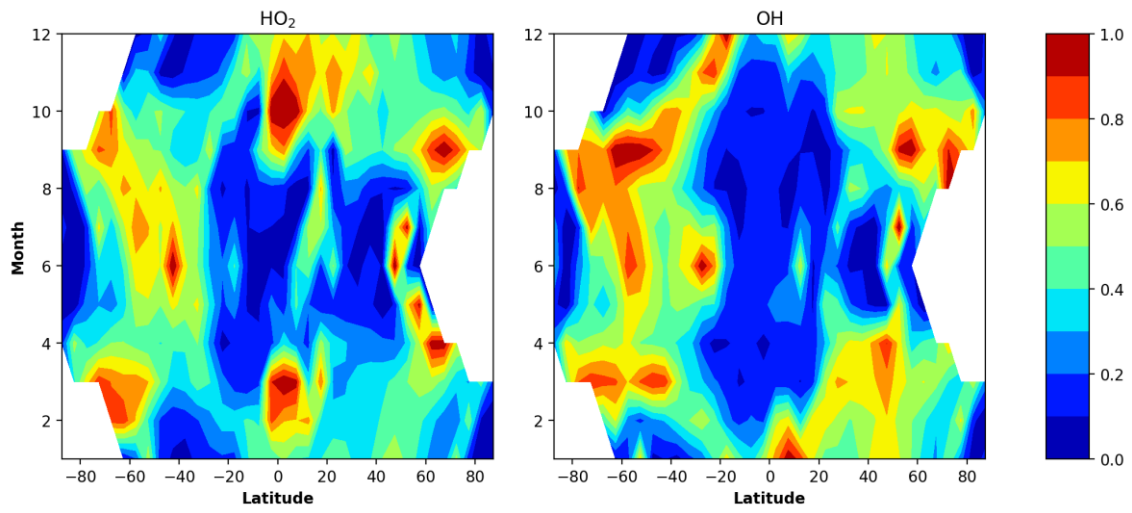


741

742 Figure 7. Nighttime mean and monthly averaged OH/OH_{sh}^{eq} . Black line shows the boundary of OH
 743 equilibrium according to condition (1). Magenta line shows $\langle Crit_{OH} \rangle = 0.1$, dotted white line shows
 744 $\langle Crit_{OH}^m \rangle = 0.1$.

745

746



747

748

749

750

Figure 8. Monthly and longitudinally mean of total uncertainties in determination of the local heights of the OH and HO₂ equilibrium boundaries according to the criteria (17) and (25). The white color indicates the absence of data due to polar day.